Eur. Phys. J. C (2026) 86:302
https://doi.org/10.1140/epjc/s10052-026-15496-4

THE EUROPEAN PHYSICAL JOURNAL C

Regular Article - Theoretical Physics

Wormhole solutions under tidal force constraints in $f(Q)$ gravity: a unified approach

Sweeti Kiroriwal[1,a], **S. K. Maurya**[2,3,b], **Jitendra Kumar**[1,c]

[1] Department of Mathematics, Central University of Haryana, Jant-Pali, Mahendergarh, India
[2] Department of Mathematical and Physical Sciences, College of Arts and Sciences, University of Nizwa, Nizwa, Sultanate of Oman
[3] Research Center of Astrophysics and Cosmology, Khazar University, 41 Mehseti Street, AZ1096 Baku, Azerbaijan

Received: 12 September 2025 / Accepted: 23 February 2026

Abstract This article explores traversable wormhole geometries obtained in the context of the symmetric teleparallel gravity theory and highlights their distinctive physical characteristics. Our methodology involves determining the tidal force by employing a specified form of the shape function along with an appropriate equation of state for Case I. In order to extract the shape functions associated with the wormhole solution, we apply the null-complexity condition with tidal force in Case II. In Case III, we utilize the balancing Tolman–Oppenheimer–Volkoff equation in conjunction with a tidal force to obtain viable wormhole shape function. The analysis focuses on the dependence of wormhole characteristics on the parameter ζ. The energy conditions are examined within their respective validity domains for various ranges of the model parameters. We also calculate, the volume integral quantifier, the extent of exotic matter needed to uphold the traversable wormhole structure. Through the effective potential for timelike geodesics, the influence of angular momentum on trajectories is clarified, and the corresponding deflection angle evaluation points to significant light bending close to the throat. By introducing small radial perturbations around the equilibrium shell radius, we examine the stability characteristics for all considered shape functions.

1 Introduction

Wormholes are fascinating constructs in theoretical physics, imagined as tunnels through spacetime that could link either distant regions of our universe or entirely different universes. Though extensively studied, their true nature and feasibility remain open questions in modern physics. Flamm [1] was the pioneer in proposing the idea of a wormhole (WH). Subsequently, in 1935, Einstein and Rosen introduced the notion of "WHs" or "bridges." The Einstein–Rosen WH was initially regarded as non-traversable, as its throat underwent rapid collapse and expansion, preventing even light from crossing from one region to the other [2]. The term "WH" was initially used by Misner [3] and Wheeler [4] in 1957 to refer to these objects, which they defined as spaces with several interconnected topologies. Though, Fuller and Wheeler showed in 1962 that the Einstein–Rosen WH is unstable because no time-like particle, including light, can pass through this region [5]. It has been suggested by Ellis [6] that a phantom scalar field could provide the necessary conditions to support a traversable WH. Kar explored static WHs by analyzing various examples and their characteristics [7]. Later, a traversable WHs physical acceptability was guaranteed by Morris and Thorne. This revitalized interest among the researchers in the field in 1988 [8]. In their analysis, they considered static, spherically symmetric space-time geometries to explore the properties and feasibility of such structures. Subsequently, Poisson and Visser [9] extended this work by proposing a type of WH called a thin-shell WH. This model involves connecting two separate manifolds by cutting and joining them, thereby forming a new space-time structure. Morris and Thorne [8] pointed out that WH solutions of this type cannot satisfy the null energy condition, thus requiring exotic matter. This matter, which violates conventional energy laws, possesses unusual features, including the hypothetical existence of particles with negative mass. The existence of WHs has been studied extensively in [10], and numerous works have focused on the stability of traversable WHs. In particular, Shinkai and Hayward [11] showed via numerical simu-

[a] e-mail: sweeti222020@cuh.ac.in
[b] e-mail: sunil@unizwa.edu.om (corresponding author)
[c] e-mail: jitendark@gmail.com (corresponding author)

Published online: 24 March 2026

lations that Ellis WHs are unstable. While general relativity (GR) has been instrumental in understanding the universe, the phenomenon of accelerated expansion reveals limitations that motivate the search for other theoretical models [12,13]. This has led to the development of several modified gravitational theories, among which $f(R)$ gravity [14], $f(R,T)$ gravity [15], and $f(Q)$ gravity [16] are prominent examples. These frameworks provide deeper insights into cosmological dynamics and the formation of astrophysical structures. In this paper, we discuss our analysis of WH geometries in the $f(Q)$ gravity theory.

The $f(Q)$ gravity framework emerges from new classes of modified gravity theories, derived from symmetric teleparallel gravity and formulated in terms of the non-metricity scalar Q. Jimenez et al. [16] introduced the $f(Q)$ gravity theory, which employs the nonmetricity scalar Q to describe gravitational influence. Over the past few years, $f(Q)$ gravity has been subjected to extensive observational tests. Lazkoz et al. [17] explored the observational constraints on $f(Q)$ gravity, employing diverse datasets including Type Ia supernovae, Hubble rate observations, quasars, baryon acoustic oscillations, gamma-ray bursts, and the cosmic microwave background. Mandal and his associates [18] analyzed the theory from a theoretical perspective: by developing a novel embedding technique that incorporates nonmetricity effects, they established that $f(Q)$ models satisfy the energy conditions and thus remain consistent with fundamental physical principles. These investigations significantly advance the understanding of $f(Q)$ gravity as a viable alternative to conventional gravitational frameworks and open new directions for exploring foundational gravitational concepts and their cosmological implications. Gadbail and his collaborators [19] reconstructed $f(Q)$ gravity using the FLRW metric, recovering the ΛCDM expansion and showing that general Q functions require extra degrees of freedom of matter. In parallel, Hassan et al. [20] investigated Casimir WH spacetimes under the Generalized Uncertainty Principle (GUP) within $f(Q)$ gravity, analyzing two forms of $f(Q)$ and providing analytic as well as numerical solutions. Their results, which incorporate GUP effects, include a detailed analysis of the ADM mass and calculations involving volume integrals to identify the exotic matter required at the WH throat. Mustafa et al. [21] applied the embedding class one criteria within the $f(Q)$ gravity framework to obtain WH solutions that satisfy the energy conditions.

The impact of $f(Q)$ gravity on cosmology has been the subject of considerable research, with many works addressing its role and potential applications. In particular, Harko and colleagues [22] made use of this theory to explore a variety of cosmological aspects. Moreover, Anagnostopoulos et al. [23] applied Big Bang Nucleosynthesis principles in conjunction with observational data to constrain different categories of $f(Q)$ models.

There are various modified gravity theories in which the WH solution was discussed. Sahoo et al. discussed about Casimir WH in $f(Q,T)$ gravity [24]. Banerjee et al. examined a class of WH solutions by taking different functional forms in $f(Q)$ gravity [25]. Lobo et al. [26,27] considered a specific WH shape function and equation of state (EoS) in $f(R)$ gravity. Rahman et al. [28] construct a novel class of five-dimensional (5D) thin-shell WHs using the cut-and-paste technique applied to black hole solutions in Einstein—Gauss–Bonnet gravity. Kalam et al. [29] investigate WH solutions in the halos of dwarf and massive spiral galaxies by using observed flat rotation curves as input.

In [30], Malik and collaborators explore traversable WH solutions in the context of $f(R)$ gravity, making use of the Karmarkar condition. Bhar and her colleagues [31] analysed the WH solution in dRGT gravity theory in the background of non-commutative geometry by considering Gaussian and Lorentzian distributions. In the case of weak gravitational fields, Falco et al. [32] developed a method for reconstructing WH solutions using extended theories of gravity. There are also numerous investigations in different frameworks of gravity, including $f(T)$ gravity [33], $f(G)$ gravity [34], Brans–Dicke theory [35–38]. Rahaman et al. [39] present the theoretical construction of a $(2+1)$ dimensional rotating thin-shell WH within the framework of the Darmois–Israel junction formalism. In Ref. [40], Kalam et al. investigated the feasibility of constructing a traversable WH in the Randall–Sundrum braneworld scenario supported by non-exotic matter through the use of the Kuchowicz gravitational potential. From a geometric viewpoint, WHs in $f(Q)$ gravity differ fundamentally from those in $f(R)$ and $f(T)$ frameworks. In $f(R)$ gravity, the gravitational interaction is governed by spacetime curvature, which generally leads to fourth-order field equations and introduces additional scalar degrees of freedom that strongly influence the WH geometry and the degree of energy-condition violation [26]. In contrast, $f(Q)$ gravity is formulated within symmetric teleparallel geometry, where curvature and torsion vanish identically and gravity is entirely described by the non-metricity scalar Q. As a result, the field equations remain second order, making the theory dynamically simpler and closer to GR at the level of differential structure [16]. Compared to $f(T)$ gravity, where WH solutions may depend on the choice of tetrads and can suffer from local Lorentz invariance issues [33], $f(Q)$ gravity admits a fully covariant formulation. Physically, this implies that WH configurations in $f(Q)$ gravity are supported by purely non-metric effects, allowing the effective geometric contributions to play the role of exotic matter near the throat. Consequently, the violation of the null energy condition can be attributed to the gravitational sector itself rather than to the physical matter content [41].

This paper is structured in the following manner. In the introduction Sect. 1, we include a literature review related to

$f(Q)$ gravity. Section 2 is devoted to the formulation of the field equations. Section 3 discusses WH shape functions and non-zero tidal forces by using different approaches. Section 4 examines the stability of the solutions by employing energy conditions, embedding diagrams, volume integral quantifier, effective potential, and deflection angles. The conclusions are presented in Sect. 5.

2 Geometric aspects in $f(Q)$ gravity

The governing action for symmetric teleparallel gravity is expressed by [42]

$$S = \frac{1}{2}\int f\,\sqrt{-g}\;d^4x + \int \mathrm{L}_m\,\sqrt{-g}\;d^4x, \tag{1}$$

where, f denotes a function of the non-metricity scalar Q, with $g = \det(g_{\mu\nu})$ denoting the determinant of the spacetime metric, whereas L_m refers to the matter Lagrangian density.

The non-metricity tensor together with its corresponding traces are defined as follows [16,43]

$$Q_{\lambda\mu\nu} = \nabla_\lambda g_{\mu\nu}, \tag{2}$$

$$Q_a = Q^{\mu}{}_{\mu a}, \quad \tilde{Q}_a = Q^{\mu}_{a\mu}. \tag{3}$$

With reference to the non-metricity tensor, the superpotential $P^{\alpha}_{\mu\nu}$ takes the following form

$$P^{\alpha}_{\mu\nu} = \frac{1}{4}\Big[-Q^{\alpha}_{\mu\nu} + Q^{\alpha}g_{\mu\nu} - \tilde{Q}^{\alpha}g_{\mu\nu} + 2\,Q_{(\mu}{}^{\alpha}{}_{\nu)} - \delta^{\alpha}_{(\mu}Q_{\nu)}\Big] \tag{4}$$

where the trace associated with the non-metricity tensor is

$$Q = -Q_{\alpha\mu\nu}P^{\alpha\mu\nu}, \tag{5}$$

which is known as the non-metricity scalar.

Consequently, the energy-momentum tensor representing the matter within space-time takes the form.

$$T_{\mu\nu} = -\frac{2}{\sqrt{-g}}\frac{\delta\left[\sqrt{-g}\,\mathrm{L}_m\right]}{\delta g^{\mu\nu}}. \tag{6}$$

Upon taking the variation of action (1) relative to $g_{\mu\nu}$, one arrives at

$$T_{\mu\nu} = \frac{-2}{\sqrt{-g}}\nabla_\gamma\left(\sqrt{-g}f_Q P^{\gamma}_{\mu\nu}\right) - \frac{1}{2}g_{\mu\nu}f - f_Q\left(P_{\mu\gamma\iota}Q_{\nu}{}^{\gamma\iota} - 2Q_{\gamma\iota\mu}P^{\gamma\iota}_{\nu}\right), \tag{7}$$

and

$$\nabla_\mu\nabla_\nu\left(\sqrt{-g}f_Q P^{\nu}_{\mu\gamma}\right) = 0, \tag{8}$$

where $f_Q = \frac{df(Q)}{dQ}$.

2.2. Traversable WH configuration: metric structure and energy conditions

The line element for a traversable WH with static and spherical symmetry is given by the Morris–Thorne metric [44–50]

$$ds^2 = -e^{2\Phi}dt^2 + \frac{1}{1-\frac{R_S}{r}}dr^2 + r^2 d\Omega_2^2, \tag{9}$$

where $d\Omega_2^2 = d\theta^2 + \sin^2\theta\,d\phi^2$, and Φ corresponds to the redshift function, which varies solely with the radial coordinate, defined in the domain $r_0 \le r < \infty$. Here, r_0 stands for the radius associated with the throat of the WH. The quantity $e^{2\Phi(r)}$ must remain finite throughout the spacetime to prevent the formation of event horizons or singularities. The redshift function Φ governs the gravitational redshift observed by distant observers and characterizes the radial tidal forces. The spatial profile of the WH is determined through the shape function $R_S(r)$. The subsequent conditions must be satisfied

1. The shape function is constrained at the throat of the WH by $R_S(r_0) = r_0$, and it should obey $R_S(r) < r\ \forall\ r > r_0$.
2. The *flaring-out condition* requires that the expression $\frac{rR_S' - R_S}{R_S'}$ remains negative, where $R_S' = \frac{dR_S}{dr}$.
3. To ensure *asymptotic flatness*, the ratio $\frac{R_S}{r}$ must approach zero in the limit $r \to \infty$.

The physical viability of a WH solution can be evaluated through the energy conditions: Null Energy Condition (NEC), Strong Energy Condition (SEC), Dominant Energy Condition (DEC), Trace Energy Condition (TEC), and Weak Energy Condition (WEC), which are presented below [51].

1. **NEC:** Requires $0 \le \rho + P_r$ and $0 \le \rho + P_t$.
2. **WEC:** Demands $0 \le \rho$, $0 \le \rho + P_r$, and $0 \le \rho + P_t$.
3. **WEC:** Ensures $0 \le \rho - P_r$ and $0 \le \rho - P_t$.
4. **TEC:** Ensures $0 \le \rho - P_r - 2P_t$.
5. **SEC:** Implies $0 \le \rho + P_r$, $0 \le \rho + P_t$, and $0 \le \rho + P_r + 2P_t$.

The condition of having a minimum throat radius, along with traversability constraints, gives rise to a negative pressure at the WH throat. This effect is balanced by the violation of the NEC, i.e. $\rho + P_r < 0$, which can be expressed equivalently as

$$\frac{(rR_S' - R_S)}{R_S'} < 0, \tag{10}$$

is fundamentally linked to the traversability of WHs. Moreover, the Raychaudhuri equation (RE) plays a crucial role in analyzing WH traversability and its relationship with the violation of energy conditions in GR. The RE governs the evolution of a congruence of null geodesics and is expressed as [52]

$$\rho = \frac{(r-R_S)}{2r^3}\left[\frac{r^3 f}{r-R_S} + f_Q\left(\frac{R_S\left(r\Phi'+2\right)}{r-R_S} + \frac{(2r-R_S)\left(rR'_S-R_S\right)}{(r-R_S)^2}\right) + \frac{2rR_S f_{QQ}Q'}{r-R_S}\right], \tag{11}$$

$$P_r = -\frac{(r-R_S)}{2r^3}\left[\frac{r^3 f}{r-R_S} + f_Q\left(\frac{R_S}{r-R_S}\left(\frac{rR'_S-R_S}{r-R_S} + r\Phi' + 2\right) - 2r\Phi'\right) + \frac{2rR_S f_{QQ}Q'}{r-R_S}\right], \tag{12}$$

$$P_t = -\frac{(r-R_S)}{4r^2}\left[\frac{2r^2 f}{r-R_S} + f_Q\left(\frac{2(2R_S-r)\Phi'}{r-R_S} + \frac{(rR'_S-R_S)}{r(r-R_S)}\left(\frac{2r}{r-R_S} + r\Phi'\right) - r(\Phi')^2 - 2r\Phi''\right)\right.$$
$$\left. -2rf_{QQ}Q'\Phi'\right], \tag{13}$$

$$\frac{\cot\theta}{2} f_{QQ}Q' = 0. \tag{14}$$

As shown in Eq. (14), the off-diagonal contribution can be derived by employing the strategy outlined by Zhao [53], under the assumptions of a vacuum state, where $T_{\mu\nu} = 0$ and the affine connection vanishes. Substitution of the diagonal energy-momentum components into the field equations directly gives $f_{QQ} = 0$. This result reveals the essential difference between linear and nonlinear models of $f(Q)$: the linear case preserves the conservation law, while nonlinear extensions generally violate it. Moreover, Wang et al. [54] proved that the Schwarzschild solution is recovered only when it $f(Q)$ is linear. Therefore, in what follows, we focus on the linear $f(Q)$ framework, which guarantees compatibility with both energy conservation and the standard vacuum solutions of GR.

$$f_{Q,Q} = 0 => f(Q) = \zeta Q + \xi, \tag{15}$$

where ζ represents the effective coupling strength between the non-metricity scalar Q and the spacetime geometry. In particular, $\zeta = 1$ corresponds to the symmetric teleparallel equivalent of GR, while deviations from this value quantify the influence of modified gravity effects. The constant term ξ plays a role analogous to a cosmological constant, contributing an effective vacuum energy density that can significantly affect the global geometry and stability of the WH spacetime. For the specific choice $\zeta = 1$ and $\xi = 0$, the model exactly reduces to the symmetric teleparallel equivalent of GR, as the non-metricity scalar Q governs the gravitational dynamics in a manner analogous to the Ricci scalar R in standard GR

$$\rho = \frac{\xi}{2} - \frac{\zeta R'_S}{r^2}, \tag{16}$$

$$P_r = \zeta\left(\frac{R_S}{r^3} - \frac{2\left(1-\frac{R_S}{r}\right)\left(\Phi'\right)}{r}\right) - \frac{\xi}{2}, \tag{17}$$

$$P_t = \zeta\left((1-\frac{R_S(r)}{r})\left[\Phi'' + \Phi'^2 + \frac{R_S - rR'_S}{2r^2(1-\frac{R_S}{r})}\Phi'\right.\right.$$
$$\left.\left. + \frac{R_S - rR'_S}{2r^3(1-\frac{R_S}{r})} + \frac{\Phi'}{r}\right]\right) - \frac{\xi}{2}. \tag{18}$$

3 Wormhole solutions

3.1 Case I: construction of red shift function by using EoS-based approach

Various techniques allow probing of WH geometry, including placing restrictions on the energy-momentum tensor components or on related functions such as $R_S(r)$ and $\Phi(r)$. In theoretical physics, the EoS is a crucial framework for modeling the behavior of both cosmological and astrophysical structures. Particularly in WH studies, the EoS of the matter threading the WH plays a critical role. Within general relativistic theory, the EoS expresses the connection between the energy density ρ and the pressures P_r (radial) and P_t (tangential), thereby characterizing the matter sustaining the WH configuration. This parameter significantly contributes to our understanding of cosmic expansion and structure formation, with recent studies indicating that the universe continues to expand faster over time. The matter at the WH throat is modeled via the EoS parameter, which quantifies the ratio between the radial pressure P_r and the energy density ρ.

$$\rho = \psi P_r. \tag{19}$$

Putting in the required values we obtained,

$$r\left(\xi r(\psi+1) + 4\zeta\psi\Phi'(r)\right) = 2\zeta\left(R'_S(r) + \frac{R_S(r)\left(2r\psi\Phi'(r)+\psi\right)}{r}\right). \tag{20}$$

We now proceed to evaluate the tidal force using the above-established relation 20, utilizing the shape function in the specific form presented below.

$$R_S(r) = \sqrt[3]{\frac{r}{r_0}}, \tag{21}$$

where r_0 is throat radius. Now substitute the values of the shape function (21) in Eq. (20), one can obtain the redshift function (tidal force) as

$$\begin{aligned}\Phi(r) = \frac{-1}{48\zeta r_0\psi}\Bigg[&6\log\left(r_0\left(\frac{r}{r_0}\right)^{2/3}-1\right)\\ &(3\xi(\psi+1)-2\zeta r_0(3\psi+1))+3\xi r_0(\psi+1)\\ &\left(2r^2+3r\sqrt[3]{\frac{r}{r_0}}+6\left(\frac{r}{r_0}\right)^{2/3}\right)+8\zeta r_0(3\psi+1)\\ &\log\left(\frac{r}{r_0}\right)\Bigg]+c_1.\end{aligned} \tag{22}$$

By using these shape and redshift functions, we further analyze the other properties.

3.2 Case-II: shape function through null complexity with tidal force

The simplest physical systems are characterized by zero complexity, such as a perfect crystal, exhibiting perfect periodic order, or an isolated ideal gas, representing complete randomness. These examples form the foundational basis for the concept of "complexity" in physics.

The idea of defining a complexity factor within self-gravitating configurations was originally put forward by Herrera [55]. According to his theoretical construct, a fluid with uniform density and isotropic pressure constitutes a basic physical configuration, grounded in the notion that complexity is a significant physical measure. In such a case, the complexity factor is defined to be zero. A specific scalar quantity, denoted as $y_{\rm cf}$, follows from the orthogonal separation of the Riemann tensor and reflects the inherent complexity of the system. This scalar function reflects the combined effects of pressure anisotropy and energy density inhomogeneity, which both vanish for a homogeneous and isotropic fluid distribution. Interestingly, the complexity factor may also vanish in more general systems where the two contributions precisely cancel each other out. The complexity factor arises due to the combined effect of pressure anisotropy and energy density inhomogeneity. Notably, when these two contributions cancel out, a system can still exhibit a complexity factor equal to zero. In the study of static, spherically symmetric fluid configurations, Herrera proposed a method of evaluating complexity using these characteristics. The complexity can be eliminated either by assuming a homogeneous and isotropic matter distribution or by ensuring that pressure anisotropy cancels out the density inhomogeneity. This requirement aids in simplifying the governing field equations by imposing the condition that the complexity factor vanishes throughout the interior. The model's metric function can then be selected on the basis of physical reasoning. This leads to the construction of a new bridge equation through the vanishing complexity condition, which links different metric components. To establish this relation, we utilize the complexity factor ($y_{\rm cf}$) as defined by Herrera.

For spherically symmetric space-times, Herrera proposed the concept of a complexity factor [56]. It is defined as

$$y_{\rm cf} = \Pi - \frac{1}{2r^3}\int_0^r r^3\frac{d\rho(r)}{dr}\,dr. \tag{23}$$

Here $\Pi = P_r - P_t$. According to this formulation, the complexity factor $y_{\rm cf}$ vanishes for an isotropic and homogeneous matter distribution. The above expression encapsulates key geometric features of the WH, as discussed in [57].

We intend to generate a WH solution through the enforcement of the zero-complexity constraint.

With the help of Eqs. (16)–(18), $y_{\rm cf}$ can be expressed as

$$\begin{aligned}y_{\rm cf} =\ &\frac{\zeta\left(r^2R_S'-3rR_S\right)}{2r^3}+\frac{1}{2r^3}\\ &\Bigg[\zeta\Bigg(r\left(r\left(r^2\Phi'+1\right)R_S'-2r\left(r^3\left(\Phi'\right)^2\right.\right.\\ &\left.+r^2\Phi''+3r\Phi'\right)\Bigg)+rR_S\Big(2r^4\left(\Phi'\right)^2+2r^3\Phi''\\ &\left.+5r^2\Phi'+1\right)\Bigg)\Bigg].\end{aligned} \tag{24}$$

Considering the vanishing of the complexity factor condition, i.e., $y_{\rm cf}=0$, we obtain

$$\begin{aligned}y_{\rm cf} =\ &\zeta\left(-2r\left(r\left(r^2\Phi'+rr\Phi''\right)+3r\Phi'\right)\right.\\ &+r\left(rr\Phi'+2\right)R_S'+rR_S\\ &\left.\left(2r\Phi''+2r\left(r\Phi'\right)^2+5r\Phi'-\frac{2}{r}\right)\right).\end{aligned} \tag{25}$$

We choose the redshift function as

$$\Phi(r) = \frac{\eta r^2+1}{1-\beta r^2}, \qquad \beta r^2 \neq 1, \tag{26}$$

where the parameters η and β govern the gravitational redshift and tidal forces experienced by test particles. The parameter η controls the growth of the redshift function near the WH throat and is associated with the strength of tidal effects, while β characterizes the radial deformation of space-time. Appropriate bounds on β ensure the regularity of $\Phi(r)$ and prevent the formation of event horizons, thereby guaranteeing the traversability of the WH geometry.

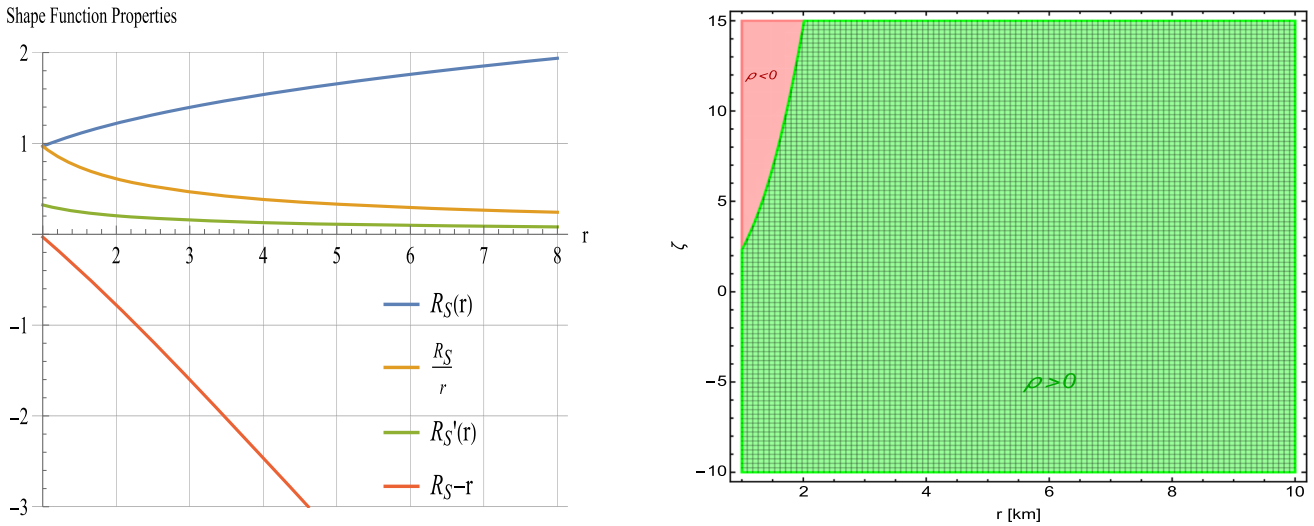

Fig. 1 Evolution of the shape function properties (left) and energy density (right) with $r_0 = 1.1$, $\xi = 1.5$, $\Psi = 0.54$, $k_1 = 0.5$ for case I

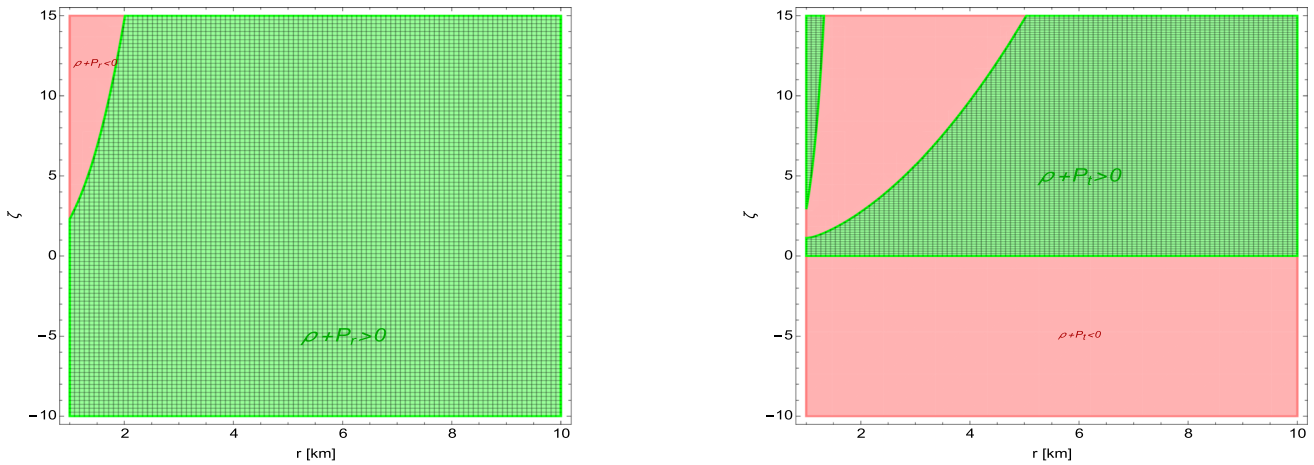

Fig. 2 Evolution of the NEC: $\rho + P_r$ (left) and $\rho + P_t$ (right) with $r_0 = 1.1$, $\xi = 1.5$, $\Psi = 0.54$, $k_1 = 0.5$ for case I

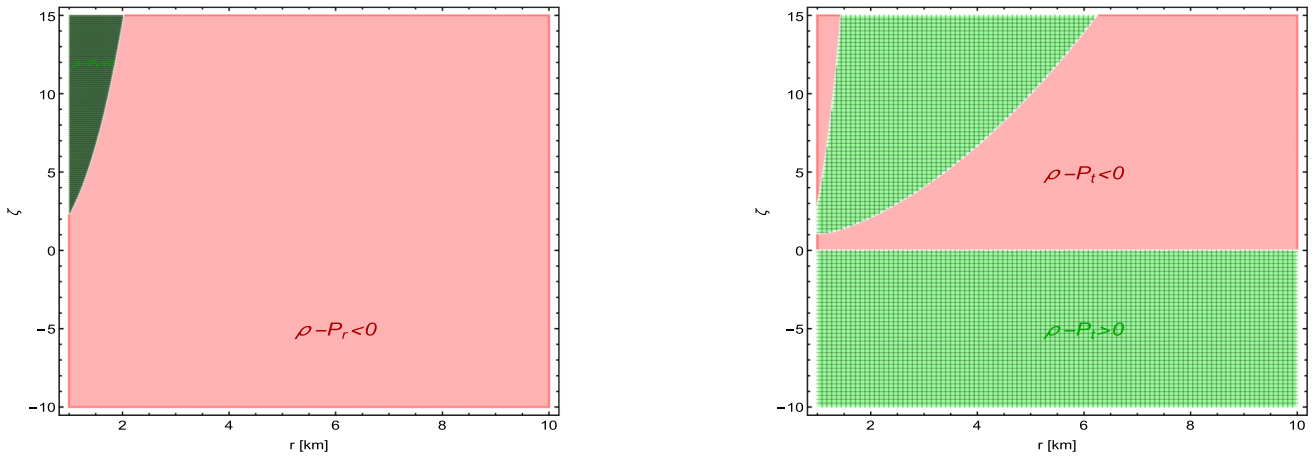

Fig. 3 Evolution of the DEC: $\rho - P_r$ (left) and $\rho - P_t$ (right) with $r_0 = 1.1$, $\xi = 1.5$, $\Psi = 0.54$, $k_1 = 0.5$ for case I

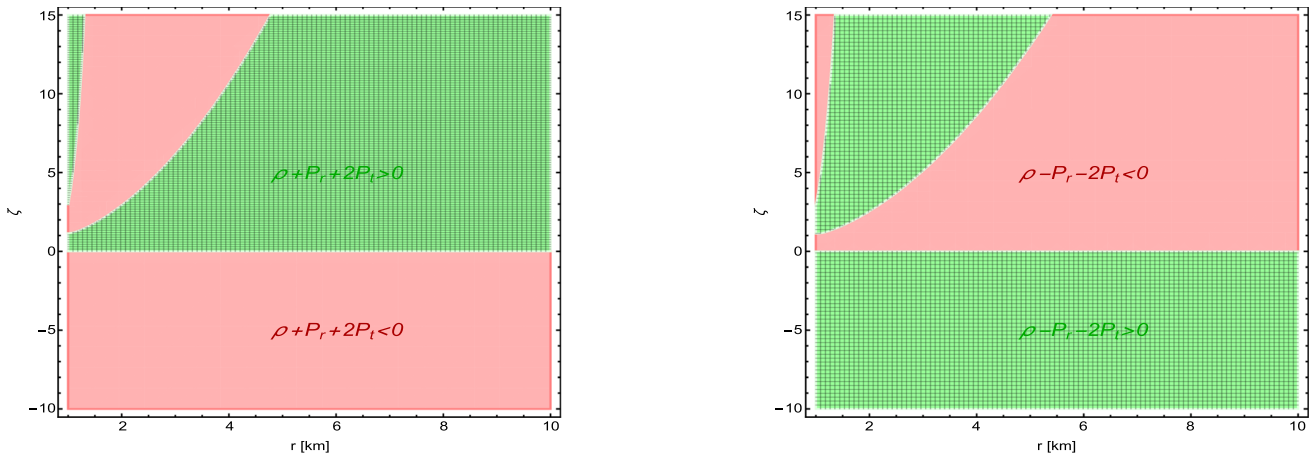

Fig. 4 Evolution of the SEC: $\rho + P_r + 2P_t$ (left) and TEC: $\rho - P_r - 2P_t$ (right) with $r_0 = 1.1$, $\xi = 1.5$, $\Psi = 0.54$, $k_1 = 0.5$ for case I

Substituting this form into Eq. (25), consequently, the shape function $\mathcal{R}_S(r)$ takes the form

$$\begin{aligned} R_S(r) \;=\; & \frac{1}{\left(\beta^2 r^4 + r^2(\eta-\beta)+1\right)^2}\Bigg(r\left(\beta r^2-1\right)^4 e^{\frac{2(\eta+\beta)}{\beta\left(\beta r^2-1\right)}} \\ & \left(k_1 + \left(\beta^4 \Gamma\left(5, \frac{2(\eta+\beta)}{\beta\left(r^2\beta-1\right)}\right)\right.\right. \\ & + \Bigg(8e^{-\frac{2(\eta+\beta)}{\beta\left(\beta r^2-1\right)}}\Big(2\eta^4\left(\beta r^2+1\right) \\ & -\beta^4\left(\beta r^2-1\right)^2\left(\beta r^2+1\right)+2\eta^2\beta^2\left(\beta^3 r^6+3\beta^2 r^4+2\right) \\ & +4\eta^3\beta\left(\beta^2 r^4+\beta r^2+1\right)+2\eta\beta^3\left(2\beta^3 r^6-3\beta^2 r^4\right. \\ & \left.\left.+4\beta r^2-1\right)\Big)\Bigg)\frac{1}{\left(\beta r^2-1\right)^3}\Bigg)\frac{1}{16\beta^2(\eta+\beta)^2}\Bigg)\Bigg)+C_2. \end{aligned} \tag{27}$$

The constant of integration is denoted by C_2. Using the throat condition $\mathcal{R}_S(r_0) = r_0$, the value of C_2 can be determined. Replacing this value in the expression yields the final shape function.

3.3 Case-III: shape function through balancing TOV with tidal force

The TOV equation, derived from Einstein's field equations, governs the hydrostatic equilibrium of spherically symmetric astrophysical bodies [58,59]. It relates pressure gradients to gravitational mass and radius, ensuring balance between gravitational collapse and internal pressure. When applied to WH scenarios, the TOV equation aids in identifying the conditions under which such structures could remain stable. This approach is often used in conjunction with modified gravity theories to examine whether exotic matter is a viable source for sustaining traversable WHs, thus offering insights into spacetime geometry beyond conventional astrophysical environments. The TOV equation is expressed as

$$\frac{dP_r}{dr} + \frac{K'(P_r+\rho)}{2} + \frac{2(P_r-P_t)}{r} = 0, \tag{28}$$

where quantity K is given by $K = 2\Phi(r)$, and $\Phi(r)$ corresponds to the redshift function. This equation encapsulates the condition for hydrostatic equilibrium in a static, spherically symmetric WH structure. It accounts for the balance among three types of forces: the gravitational force (F_{gf}), the hydrostatic force (F_{hf}), and the anisotropic force (F_{af}), which arises from the difference between radial and tangential pressures. These individual force components are defined as follows

$$\text{(i)}\quad F_g = \frac{-K'(\rho+P_r)}{2}, \qquad \text{(ii)}\quad F_a = \frac{2(P_t-P_r)}{r} \qquad \text{and}$$
$$\text{(iii)}\quad F_h = -\frac{dP_r}{dr}.$$

For the WH to remain in a state of equilibrium, the sum of these three forces must vanish.

$$F_{\text{ts}} = F_{gf} + F_{af} + F_{hf} = 0. \tag{29}$$

This condition ensures a physically stable WH configuration under the joint influence of gravitational attraction, pressure gradients, and anisotropic stresses. Now, our aim is to obtain a WH shape function by applying the zero TOV condition. Utilizing Eqs. (16)–(18), the expression for F_{ts} is derived as

$$\begin{aligned} F_{\text{ts}} \;=\; & \frac{1}{r^4}\Bigg(2\zeta\left(r\left(r\left(r^2\Phi'+1\right)R_S' - 2r\left(r^3\left(\Phi'\right)^2 + r^2\Phi'' + r\Phi'\right)\right)\right. \\ & \left.+ r R_S\left(2r^4\left(\Phi'\right)^2 + 2r^3\Phi'' + r^2\Phi' - 1\right)\right)\Bigg). \end{aligned} \tag{30}$$

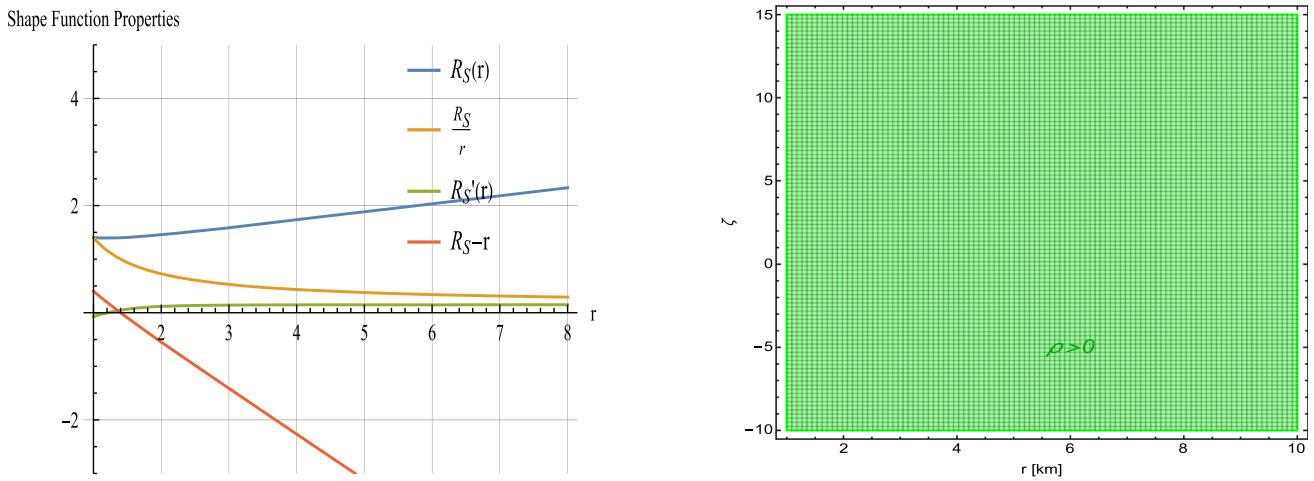

Fig. 5 Evolution of the shape function properties (left) and energy density (right) for case II with $r_0 = 1.4$, $\eta = 0.15$, $\beta = -2.03$, $k_1 = -0.85$, $\xi = 10$

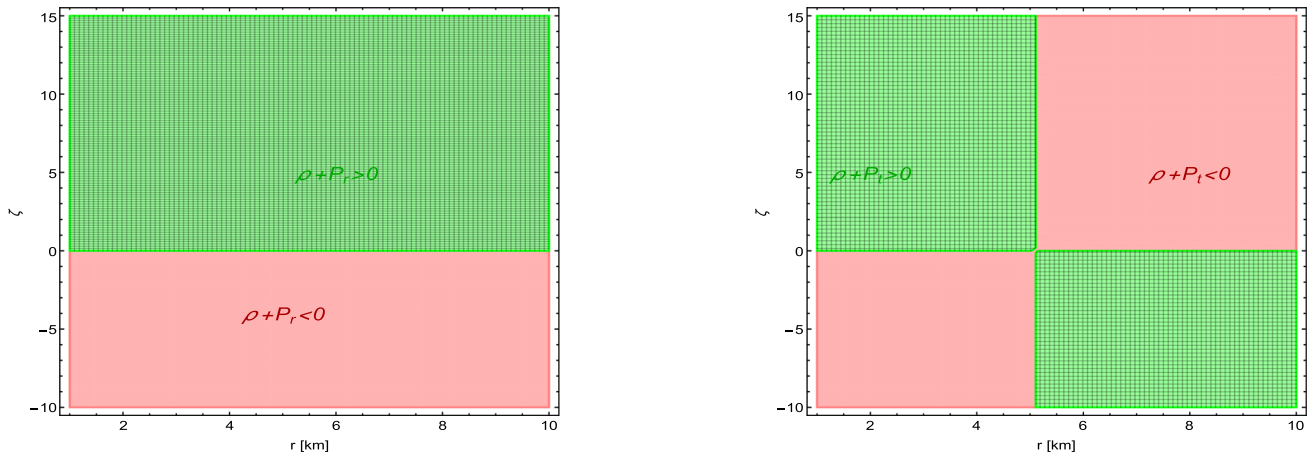

Fig. 6 Evolution of the NEC: $\rho + P_r$ (left) and $\rho + P_t$ (right) for case II with $r_0 = 1.4$, $\eta = 0.15$, $\beta = -2.03$, $k_1 = -0.85$, $\xi = 10$

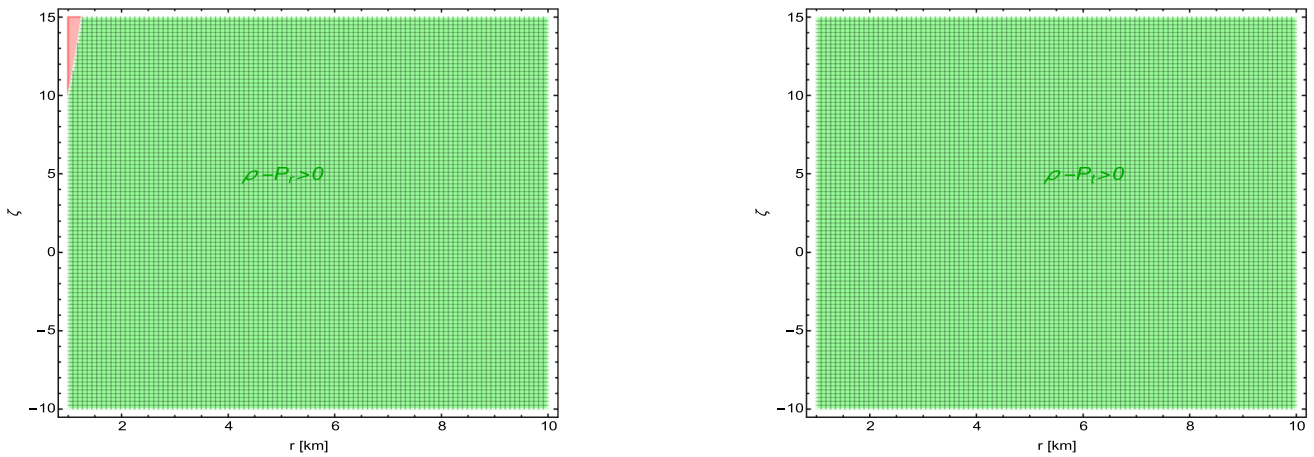

Fig. 7 Evolution of the DEC: $\rho - P_r$ (left) and $\rho - P_t$ (right) for case II with $r_0 = 1.4$, $\eta = 0.15$, $\beta = -2.03$, $k_1 = -0.85$, $\xi = 10$

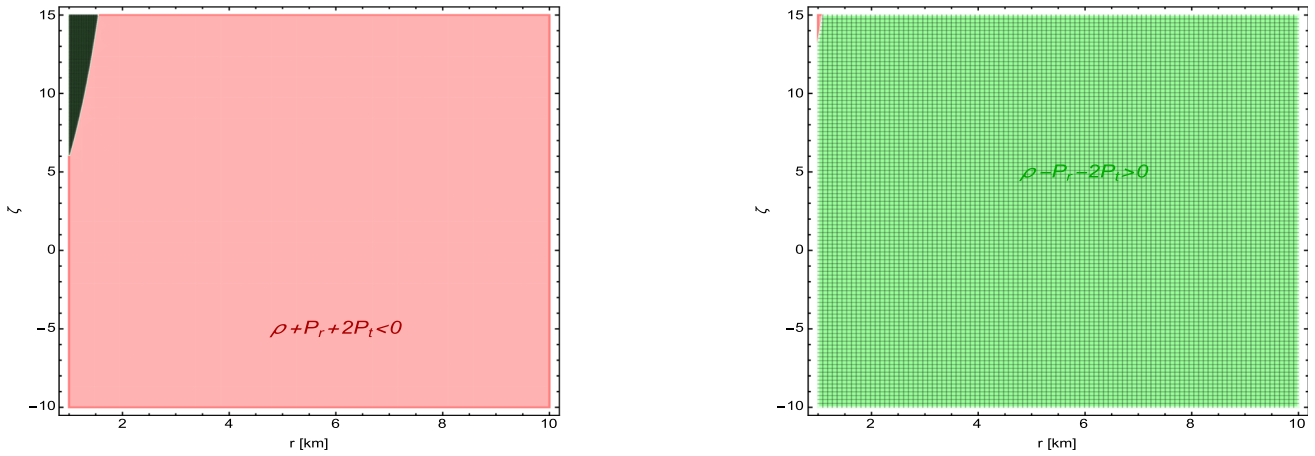

Fig. 8 Evolution of the SEC: $\rho + P_r + 2P_t$ (left) and TEC: $\rho - P_r - 2P_t$ (right) for case II with $r_0 = 1.4$, $\eta = 0.15$, $\beta = -2.03$, $k_1 = -0.85$, $\xi = 10$

To solve the above nonlinear equation, we consider the nonzero tidal force in the form

$$\Phi(r) = \frac{\eta r^2 + 1}{1 - \beta r^2}, \qquad \beta r^2 \neq 1. \tag{31}$$

Upon substituting the redshift function presented above into Eq. (30), the subsequent outcome is derived as

$$\begin{aligned} F_{\rm ts} = {} & \frac{-1}{r^4\left(\beta r^2-1\right)^4}\Bigg(2\zeta\Bigg(-r^2\left(\beta r^2-1\right)^2 \\ & \left(\beta^2 r^4+2\eta r^2+1\right)R_S' + 8r^3(\beta+\eta) \\ & \left(-\beta^2 r^4+\beta r^2+\eta r^2+1\right) \\ & + r R_S\left(\beta^4 r^8+6\beta^3 r^6-6\beta^2 r^4-8\eta^2 r^4-10\beta r^2\right. \\ & \left.+2\eta r^2\left(5\beta^2 r^4-10\beta r^2-3\right)+1\right)\Bigg)\Bigg). \end{aligned} \tag{32}$$

Under the constraint that the sum of forces is zero ($y_{\rm ts} = 0$), the shape function can be determined as,

$$\begin{aligned} R_S(r) = {} & C_3 + r\left(\sqrt{\eta^2-\beta^2}+\eta+\beta^2 r^2\right)^{-\frac{2\sqrt{\eta^2-\beta^2}+\beta+\eta}{\sqrt{\eta^2-\beta^2}}} \\ & \left(-\sqrt{\eta^2-\beta^2}+\eta+\beta^2 r^2\right)^{\frac{\beta+\eta}{\sqrt{\eta^2-\beta^2}}-2} \\ & \Bigg(k_2\left(\beta r^2-1\right)^4 e^{\frac{2(\beta+\eta)}{\beta\left(\beta r^2-1\right)}} \\ & +\beta^4\left(\beta^2 r^4+2\eta r^2+1\right)^2 \\ & \left(-\sqrt{\eta^2-\beta^2}+\eta+\beta^2 r^2\right)^{-\frac{\beta+\eta}{\sqrt{\eta^2-\beta^2}}} \\ & \left(\sqrt{\eta^2-\beta^2}+\eta+\beta^2 r^2\right)^{\frac{\beta+\eta}{\sqrt{\eta^2-\beta^2}}}\Bigg). \end{aligned} \tag{33}$$

3.4 Analysis of shape functions

Based on the shape functions derived in Eqs. (21, 27, and 33), we conducted a detailed analysis of its characteristics. This allowed us to generate plots for $R_S(r)$, $R_S(r)/r$, and $R_S(r) - r$. These plots are displayed in the left panel of Figs. 1, 5 and 9 for all cases. By carefully selecting parameter values such as $r_0 = 1.1$ for case I, $r_0 = 1.4$, $\eta = 0.15$, $\beta = -2.03$, $k_1 = -0.85$ for case II, and for case III, $r_0 = 1.25$, $\eta = 3.72$, $\beta = -1.52$, $k_2 = -4.76$, we were able to effectively construct the shape function plots. It is evident from the analysis that the shape functions grows continuously over the radial domain, and the throat occurs at $r_0 = 1.1, 1.4, 1.25$. Examining Figs. 1, 5 and 9 more closely, we observe that for $r > r_0$, the expression $R_S(r) - r$ becomes negative. This implies that $\frac{R_S(r)}{r} < 1$. In other words, as r increases, the quantity $R_S(r) - r$ decreases, satisfying the flaring-out condition for $r \geq r_0$ and ensuring that $R_S'(r)$ remains less than 1. Furthermore, the conditions $R_S'(r) < 1$ and $\frac{R_S(r)}{r} < 1$ hold true $\forall\, r > r_0$, and we also find that $\frac{R_S(r)}{r} \to 0$ as $r \to \infty$. From these observations, we deduce that the spacetime exhibits asymptotic flatness at considerable radial distances. Consequently, the shape functions derived in every scenario successfully incorporate the fundamental characteristics of WH geometries.

4 Stability criteria

4.1 Analysis of energy condition

To analyze the energy conditions, we have constructed graphs that illustrate their behavior in relation to the energy density ρ, radial pressure P_r, and tangential pressure P_t. These graphical representations are provided in Figs. 1, 2, 3, 4, 5,

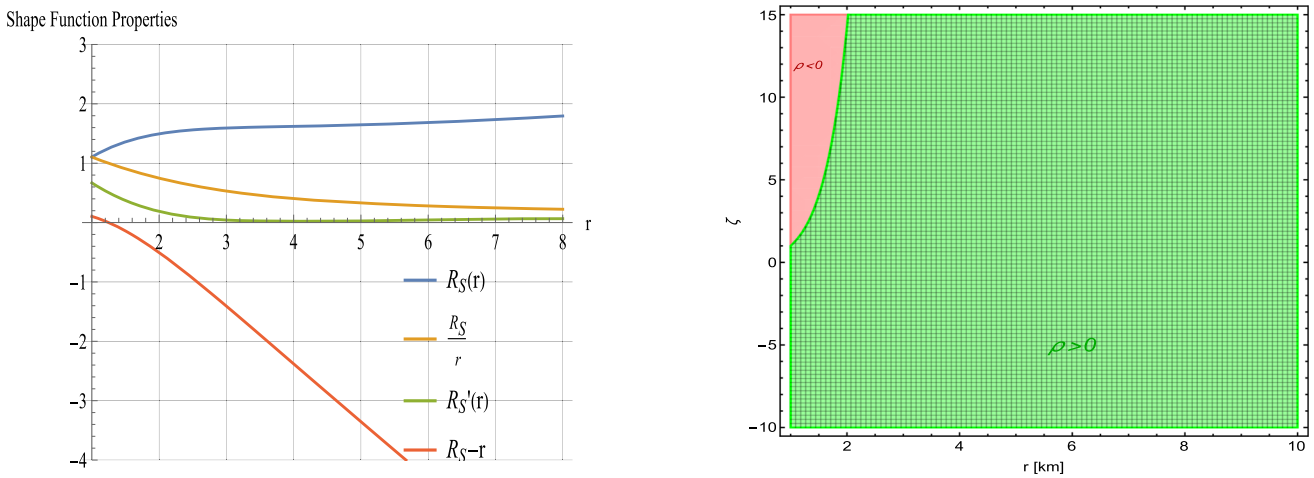

Fig. 9 Evolution of the shape function properties (left panel) and energy density (right panel) with radial coordinate for case III with $r_0 = 1.25$, $\eta = 3.72$, $\beta = -1.52$, $k_2 = -4.76$, $\xi = 1.34$

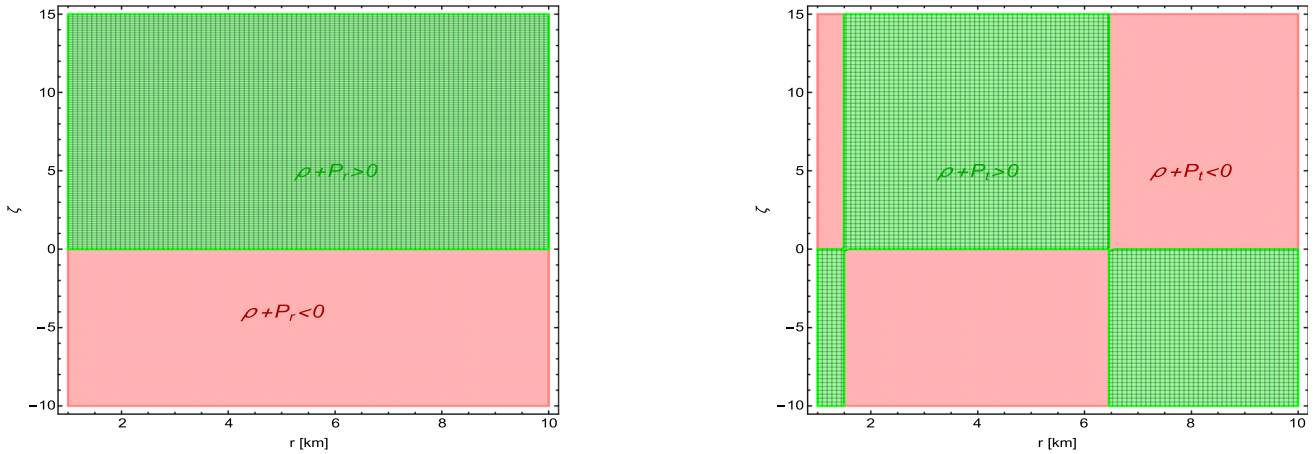

Fig. 10 Evolution of the NEC: $\rho + P_r$ (left panel) and $\rho + P_t$ (right panel) with radial coordinate for case III with $r_0 = 1.25$, $\eta = 3.72$, $\beta = -1.52$, $k_2 = -4.76$, $\xi = 1.34$

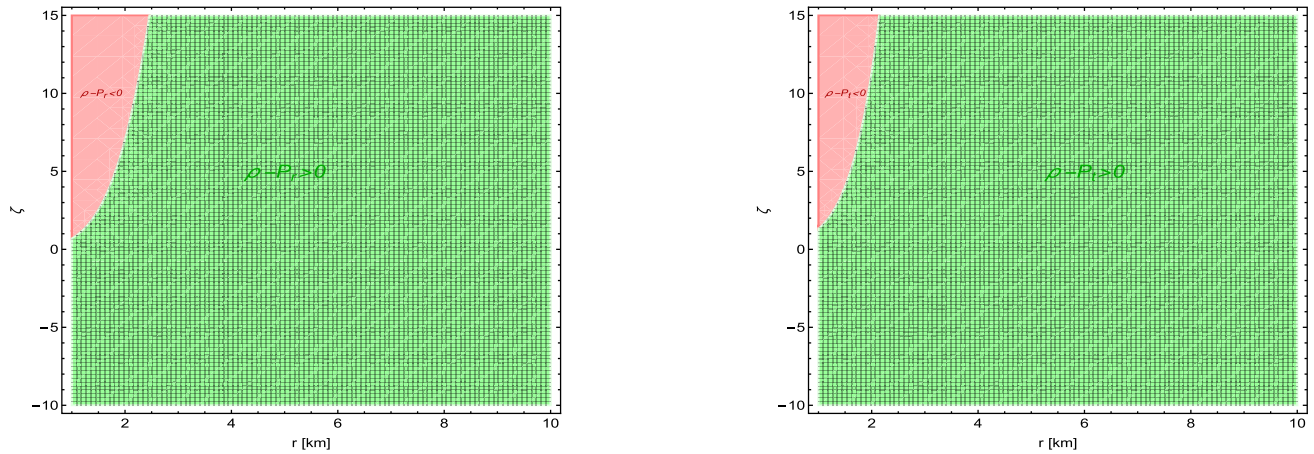

Fig. 11 Evolution of the DEC: $\rho - P_r$ (left panel) and $\rho - P_t$ (right panel) with radial coordinate for case III with $r_0 = 1.25$, $\eta = 3.72$, $\beta = -1.52$, $k_2 = -4.76$, $\xi = 1.34$

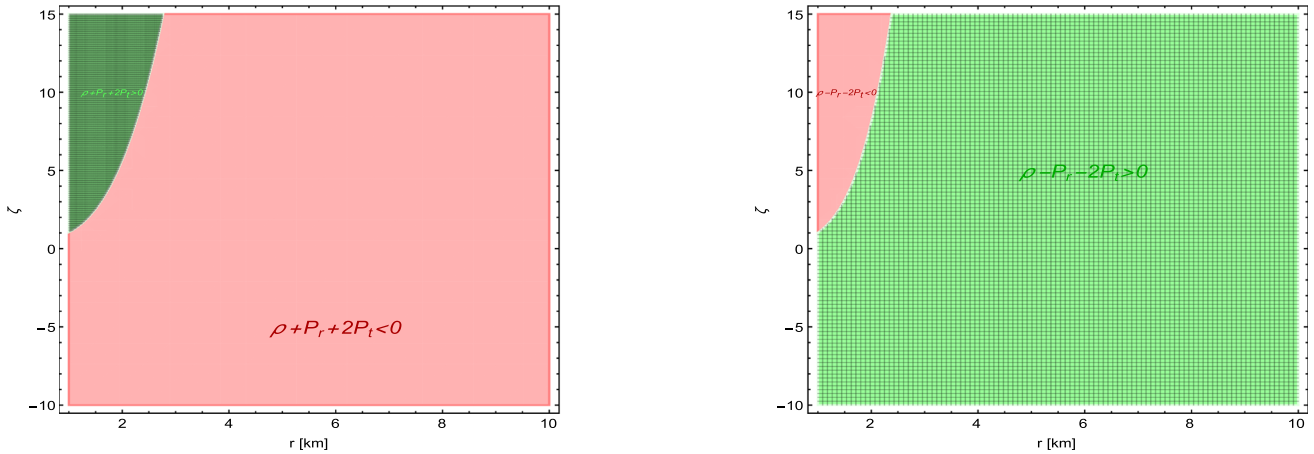

Fig. 12 Evolution of the SEC: $\rho + P_r + 2P_t$ (left panel) and TEC: $\rho - P_r - 2P_t$ (right panel) with radial coordinate for case III with $r_0 = 1.25$, $\eta = 3.72$, $\beta = -1.52$, $k_2 = -4.76$, $\xi = 1.34$

6, 7, 8, 9, 10, 11 and 12. By varying the model parameter ζ between $[-10, 15]$, we observe that all the energy conditions can attain both positive (green region) and negative (pink region) values. At $\zeta = 0$ all values are constant as $\xi/2$. This work highlights the essential contribution of exotic matter in determining the throat radius of the WH, offering a more detailed understanding of the properties of the matter that supports the WH structure.

4.1.1 Case I

- As shown in the right of Fig. 1, the energy density ρ is presented graphically as a function of the parameters r and ζ. The study reveals that ρ consistently stays positive throughout the examined range $\zeta \in [-10, 3.75]$, for specific values of the remaining free parameters. This observation is significant, as it indicates the possibility of obtaining physically reasonable matter distributions within the WH configuration. For the values of ζ that lie in $(3.75, 15]$, ρ behaves negatively near the throat, but for $r > 2$, it behaves positively. A positive energy density is essential for ensuring the stability and physical viability of WH solutions. The result implies that the matter supporting the WH prevents gravitational collapse and remains consistent with the basic energy conditions. Consequently, our findings suggest that the WH models considered here are not only of theoretical interest but may also correspond to stable and traversable geometries with physically acceptable matter content.
- The graphical analysis in Figs. 2, 3 and 4 reveals noteworthy features of the energy conditions in the vicinity of the WH throat. Our analysis shows that the condition $\rho + P_r$ behaves similarly to density behaviour. This is violated near the throat only when $\zeta \in (3.75, 15]$, whereas it is satisfied for the remaining region. On the other hand, the condition was $\rho + P_t$ violated throughout the negative range of ζ and near the throat for $\zeta \in [1.1, 15]$ but satisfied in the remaining region, which is indicated in green color. For negative values of ζ, the throat exhibits a violation of $\rho + P_t$, which reflects the failure of the NEC. This demonstrates the necessity of exotic matter in the region to uphold the WH structure and resist gravitational collapse.
- We further observed that DEC in case of $\rho - P_r$, is satisfied near the throat only when $\zeta \in (3.75, 15]$, whereas it is violated for the remaining region., as illustrated in Fig. 3 (left panel). In contrast, tangential DEC, $\rho - P_t$, is satisfied for $\zeta < 0$, but remains violated when $\zeta > 0$ and away from the throat, as depicted in Fig. 3 (right). This contrast reveals how radial and tangential pressures influence WH stability in distinct ways.
- In particular, the SEC and TEC behave opposite as each other, $\rho + P_r + 2P_t$ is violated but $\rho - P_r - 2P_t$ is satisfied for negative values of ζ as seen in Fig. 4.

4.1.2 Case II

- The graphical variation of ρ with respect to ζ and r is shown in the right of Fig. 5. The results demonstrate that ρ remains positive throughout the interval $\zeta \in [-10, 15]$, under suitable choices of the other model parameters.
- For negative values of ζ, there is a violation of the NEC in terms of the radial pressure, i.e., $\rho + P_r$, while the condition is valid for positive values of ζ. Regarding the tangential pressure $(\rho + P_t)$, a violation of the NEC occurs for negative values of ζ when $r \leq 5$, and for positive values of ζ when $r \geq 5$ as can be seen in Fig. 6. These violations of the NEC indicate the presence of exotic matter near the WH throat.

- DEC is satisfied throughout the domain, except for a small range $\zeta \in [10,\ 15]$ at the throat, in terms of $\rho - P_r$ (See Fig. 7).
- SEC is violated across most of the domain, except in a small region near the throat where $\zeta \in [5.5,\ 15]$, whereas the TEC is satisfied throughout the entire domain (See Fig. 8).

4.1.3 Case III

- As displayed in the right of Fig. 9, the profile of ρ is plotted with respect to ζ and r. It is observed that ρ remains positive within the interval $\zeta \in [-10,\ 1.1]$, for certain chosen values of the other free parameters. For $\zeta \in (1.1,\ 15]$, the energy density ρ becomes negative near the throat but turns positive for $r > 2$.
- From Fig. 10, we observe that the inequality $\rho + P_r < 0$ holds at the WH throat for negative values of ζ and positive for positive values of ζ. It is observed that $\rho + P_t > 0$ at the throat and for $r > 6.5$ when $\zeta < 0$, whereas for $\zeta > 0$ the requirement is met only within $r \in [1.5, 6.5]$. Elsewhere, the inequality is violated.
- Furthermore, DEC is seen to be violated at the WH throat for positive values of ζ with $r < 2$ and satisfied all other remaining regions as illustrated in Fig. 11.
- The SEC and TEC behave oppositely. For positive values of ζ with $r < 2.5$, SEC is violated, but TEC is satisfied. For other regions throughout the negative values of ζ and positive values of ζ with $r \geq 2.5$, SEC is violated and TEC is satisfied, as can be seen in Fig. 12.

By carefully examining the energy conditions, one gains meaningful insights into the intrinsic behavior of matter across the universe. The results of our investigation offer significant contributions to WH theory, particularly emphasizing the necessity of exotic matter for their formation and stability.

4.2 Visualization of WH geometry via embedding diagram

In this section, we study the embedding surface diagrams linked to newly derived WH shape functions under the assumptions $\theta = 2\pi$ and $t = \text{const}$. These diagrams visually represent the geometry of the WH tunnel connecting two distinct regions in spacetime, enabling a direct traversal between its mouths. Based on these assumptions, the induced metric is given by

$$ds^2 = \left(1 - \frac{R_S(r)}{r}\right)^{-1} dr^2 + r^2 d\phi^2. \tag{34}$$

The corresponding 3-dimensional Euclidean spacetime representation becomes

$$\begin{aligned} ds^2 &= r^2 d\Phi^2 + \left(1 + \left(\frac{dz}{dr}\right)^2\right) dr^2 \\ &= dt^2 + dr^2 + r^2 d\phi^2. \end{aligned} \tag{35}$$

By comparing Eqs. (34) and (35), we derive the key equation for generating the embedding diagrams of the WH

$$z'(r) = \pm \frac{1}{\sqrt{\frac{r}{R_S(r)} - 1}}, \tag{36}$$

where $'$ denotes derivative with respect to r.

In our analysis, we adopt the technique established by Marolf [60], along with the method proposed by Peter and David in [61], to construct the embedding diagrams. Due to the complexity of the newly obtained shape functions, a closed-form expression for $z(r)$ is not feasible from Eq. (36). Thus, we solve Eq. (36) numerically. Using the input parameters and throat radius for both WH models, we numerically generate the corresponding embedding diagrams, which are presented in Fig. 13 for all models, respectively.

4.3 Amount of exotic matter

The "volume integral quantifier," which evaluates the integrated amount of exotic matter sustaining a WH, is outlined in this section. Its formulation involves only the energy density ρ together with the radial pressure P_r, and is expressed as the integral

$$I_V = \oint (\rho + P_r) dV = \int_{r_0}^{\infty} 2\ (\rho + P_r) dV, \tag{37}$$

which can be further simplified as

$$I_V = \int_{r_0}^{\infty} 8\pi\ (\rho + P_r) r^2 dr. \tag{38}$$

As stated earlier, this volume integral reveals the total quantity of exotic matter in the spacetime. To determine this integral for a specific shape function $R_S(r)$, we introduce a finite cutoff radius r_1, such that the WH spans the region from r_0 to r_1. The integral is then evaluated over this finite domain. The radial coordinate r_1 is introduced as a cutoff, characterizing the WH's span from its throat r_0 to some radius $r_1 \geq r_0$. The integral must vanish in the limit $r_1 \to r_0$. In Fig. 14, the characteristics of the volume integral I_v for all cases are illustrated. The results depicted in these figures confirm that our solutions exhibit the expected behaviour. Consequently, this shows the feasibility of spacetime configurations containing WHs, which can be sustained with minimal amounts of exotic matter.

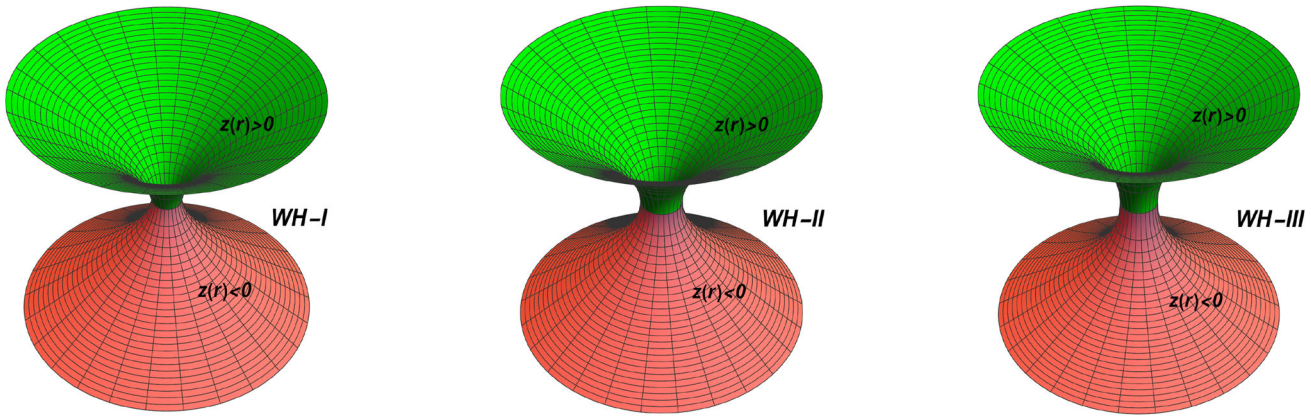

Fig. 13 Evolution of the embedding diagram for WH-I (left), WH-II (middle), and WH-III (right)

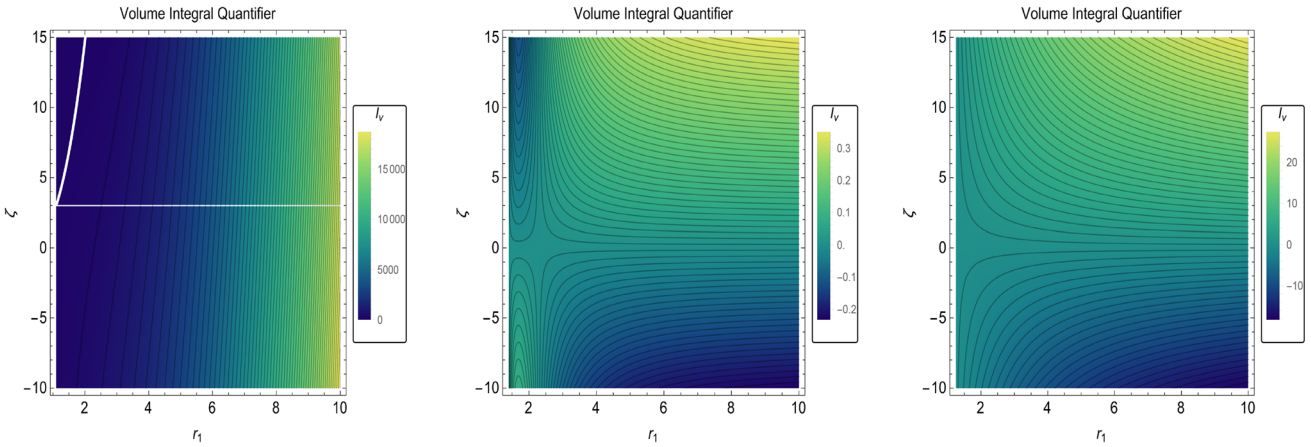

Fig. 14 Evolution of the volume integral quantifier Case I (left), Case II (middle) and Case-III (right) with radial coordinate

4.4 Deflection angle

This section examines the deflection angles generated by WHs. The curvature of space-time, produced by mass and energy, is the central factor controlling particle dynamics and the bending of light rays. In curved space-time, light rays passing near massive structures-such as black holes or WHs-are bent, even though the speed of light remains unchanged. This bending of light manifests as gravitational lensing, revealing the powerful role of gravity in determining the trajectory of light. The study of strong gravitational lensing has drawn increasing attention over the past decades, largely due to the influential work of Virbhadra and co-authors [62–64], who highlighted its applicability as a technique for exploring space-time geometry and astrophysical behavior. Continuing this framework, Bozza [65] formulated an analytical technique to analyze gravitational lensing phenomena in the strong-field limit for space-time metrics. This approach has since been widely adopted in subsequent research [66,67]. We adopt the general static, spherically symmetric geometry [68,69], whose line element is defined as

$$ds^2 = -N\,dt^2 + K\,dr^2 + C\,d\Omega^2, \tag{39}$$

where N, K, and C are functions of r.

For exploring the motion of freely falling particles in this space–time [69], the geodesic equation is utilized, linking the four–momentum $\hat{p}^\alpha$ directly to the geometry

$$\frac{d\hat{p}_\beta}{d\hat{\lambda}} = \frac{1}{2} g_{\nu\alpha,\beta}\,\hat{p}^\nu\,\hat{p}^\alpha. \tag{40}$$

The affine parameter is denoted by $\hat{\lambda}$, and it serves to parameterize photon motion along null geodesics. A fundamental property of the geodesic dynamics is that when the metric functions $g_{\alpha\nu}$ are independent of a coordinate x^β, the momentum component $\hat{p}_\beta$ is conserved. To simplify the problem, we restrict the motion to the equatorial plane ($\theta = \pi/2$). Specifically for photon trajectories, the constants of motion corresponding to the energy E and angular momentum L can be expressed in terms of the generalized momenta

as

$$\hat{p}_t = -E, \quad \hat{p}_\Phi = L.$$

The geodesic equations thus reduce to

$$\dot{t} = \frac{E}{N(r)}, \quad \dot{\Phi} = \frac{L}{C(r)}.$$

Throughout, the overdot notation is used to denote differentiation with respect to the affine parameter $\hat{\lambda}$.

The equation describing radial motion for null geodesics is

$$\dot{r}^2 = \frac{1}{K(r)}\left[\frac{E^2}{N(r)} - \frac{L^2}{C(r)}\right].$$

Introducing the impact parameter $\eta = \frac{L}{E}$ transforms this equation into

$$\left(\frac{dr}{d\Phi}\right)^2 = \frac{C(r)}{K(r)}\left[\frac{C(r)}{\eta^2 N(r)} - 1\right].$$

For a photon arriving from infinity at a polar angle $-\frac{\pi}{2} - \frac{\hat{\alpha}}{2}$ and receding back to infinity after reaching the closest distance r_0, the total bending caused by the WH geometry is determined by the deflection angle α and expressed as

$$\alpha = -\pi + 2\int_{r_c}^{\infty} \frac{e^{\Phi(r)}}{r^2\sqrt{\left(1 - \frac{R_S(r)}{r}\right)\left(\frac{1}{\beta^2} - \frac{e^{2\Phi(r)}}{r^2}\right)}}\, dr. \quad (41)$$

In this context, r_c specifies the distance of nearest approach of the photon to the WH throat, and β stands for the related impact parameter. For a null geodesic, the connection between β and r_c can be written as

$$\beta = e^{-\Phi(r_c)}\, r_c. \quad (42)$$

We proceed by employing Eq. (42) to numerically determine the deflection angle of photons in $f(Q)$ gravity. The computed results for all cases are depicted in Fig. 15. For all possible values of r_0, the calculated deflection angle assumes negative values, thereby signaling the presence of a repulsive gravitational interaction affecting the photons. This observation is consistent with previous studies, such as Panpanich et al. [70], which reported similar behavior in the corresponding spacetime. The significance of this result lies in its implication of a repulsive gravitational effect in the vicinity of the WH. Under typical circumstances, when light passes in the vicinity of massive object, gravitational attraction bends it toward the object, producing a positive deflection angle. Conversely, our finding of a negative deflection angle implies that, instead of being attracted, light is repelled from the WH. This phenomenon highlights that the gravitational features close to the WH throat differ in an essential way from the behavior typical of ordinary gravitational lensing.

4.5 Effective potential via Lagrangian formalism

The effective potential can be obtained using the Lagrangian formalism. Exploiting spherical symmetry, we fix $\theta = \pi/2$, thereby restricting the motion to the equatorial plane. Under this choice, the Lagrangian for photon motion in the WH geometry given by Eq. (9) is

$$\mathcal{L} = g_{\mu\nu}\dot{x}^\mu \dot{x}^\nu = -e^{2\Phi(r)}\dot{t}^2 + \frac{\dot{r}^2}{1 - \frac{R_S(r)}{r}} + r^2\dot{\Phi}^2, \quad (43)$$

where, an overdot denotes differentiation with respect to the affine parameter τ.

The governing Euler–Lagrange equation is expressed as

$$\frac{d}{d\tau}\left(\frac{\partial \mathcal{L}}{\partial \dot{x}^\mu}\right) - \frac{\partial \mathcal{L}}{\partial x^\mu} = 0, \quad (44)$$

leads directly to two conservation relations

$$-e^{2\Phi(r)}\dot{t} = -E, \qquad r^2\dot{\Phi} = L, \quad (45)$$

where L and E are the conserved angular momentum and energy of the test particle.

For geodesic motion, the Lagrangian Eq. (43) is constant,

$$\mathcal{L}(x^\mu, \dot{x}^\mu) = \epsilon,$$

with $\epsilon = 0$ for null geodesics and $\epsilon = -1$ for time-like geodesics [71].

Substituting into Eq. (43), one obtains

$$\frac{e^{2\Phi(r)}}{1 - \frac{b(r)}{r}}\dot{r}^2 + V^{\text{eff}} = E^2, \quad (46)$$

where V^{eff} is given by

$$V^{\text{eff}} = \left(\frac{L^2}{r^2} - \epsilon\right) \times e^{2\Phi(r)}. \quad (47)$$

In view of the fact that both factors $e^{2\Phi(r)}$ and $1 - R_S(r)/r$ are positive for $r > r_{\text{th}}$, the relationship between V^{eff} and the total energy E determines whether the particle can traverse the WH. Figure 16 illustrates V^{eff} for both null and time-like geodesics. It is evident that V^{eff} increases with L and exhibits a maximum near the throat for case II and case III. If $E^2 > V^{\text{eff}}(L, r_{\text{th}})$, the particle crosses the throat into another region. Conversely, if $E^2 < V^{\text{eff}}(L, r_{\text{th}})$, the particle returns to its original region. A turning point r_0 also exists where $\dot{r}^2 = 0$, such that $E^2 = V^{\text{eff}}(L, r_0)$, implying that a photon from infinity may be deflected at r_0 before escaping back to infinity.

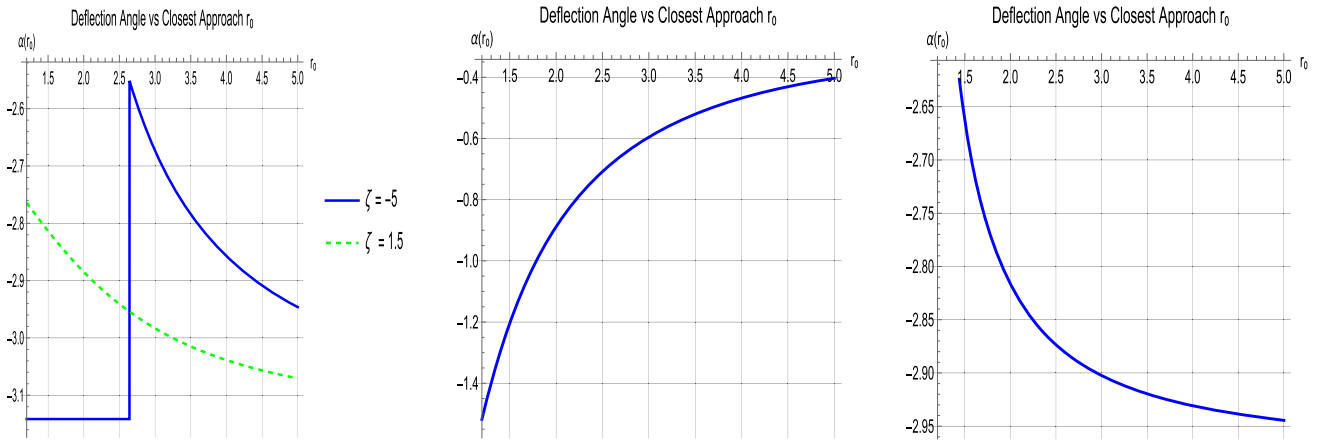

Fig. 15 Evolution of the deflection angle Case I (left), Case II (middle), and Case III (right)

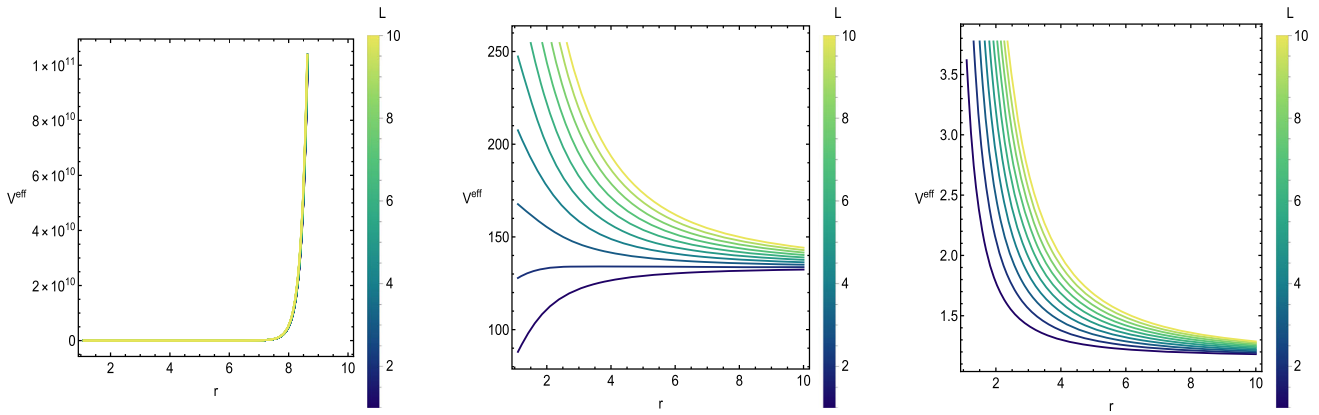

Fig. 16 Evolution of the V^{eff} potential Case I (left), Case II (middle) and Case-III (right) with radial coordinate corresponding to $\epsilon = -1$

4.6 Thin-shell around WH structure

Here, our analysis is devoted to building thin-shell structures surrounding WH spacetimes, considering two possible choices of the generic shape function under the framework of teleparallel gravity. For this purpose, the internal region is modeled as a WH manifold, while the external region is taken to be the Schwarzschild black hole spacetime. Mathematically, the line element is given by:

$$ds^2 = -\Pi_{\pm}(r_{\pm})^{-1}dr_{\pm}^2 + \Pi_{\pm}(r_{\pm})dt_{\pm}^2 - r_{\pm}^2 d\theta_{\pm}^2 - r_{\pm}^2 \sin^2\theta_{\pm} d\phi_{\pm}^2. \quad (48)$$

For the regions inside $(-)$ and outside $(+)$, the metric functions are expressed as

$$\Pi_{-}(r_{-}) = 1 - \frac{R_S(r_{-})}{r_{-}}, \quad \Pi_{+}(r_{+}) = \frac{2m}{r_{+}} + 1.$$

Following Visser's cut-and-paste method, we construct a thin shell by joining the interior WH and exterior Schwarzschild geometries at a chosen hypersurface. This technique partitions the spacetime into two domains,

$$\mathcal{M}^{\pm} = \left\{\mathbf{k} > r_h,\ r^{\pm} \leq \mathbf{k}\right\},$$

where $\mathbf{k}$ refers to the radius of the thin shell and r_h characterizes the Schwarzschild event horizon. The connection occurs along the hypersurface,

$$\Sigma = \left\{\mathbf{k} > r_h,\ r^{\pm} = \mathbf{k}\right\}.$$

It is important to ensure that the event horizon and singularity are avoided in the constructed geometry by choosing the shell radius to be larger than the event horizon radius of the Schwarzschild black hole.

Through the Darmois–Israel method, one expresses the coordinates of the manifolds and the hypersurface as

$$\eta^i = (\tau, \theta, \phi) \quad \text{and} \quad y^{\alpha} = (\tau_{\pm}, r_{\pm}, \theta_{\pm}, \phi_{\pm}),$$

respectively, where τ denotes the proper time on the hypersurface. One can connect these coordinate systems using the transformation:

$$g_{ij} = \frac{\partial y^{\alpha}}{\partial \eta^i}\frac{\partial y^{\beta}}{\partial \eta^j} g_{\alpha\beta}.$$

In parametric representation, the hypersurface is defined by

$$\Sigma : R(r,\tau) = 0 \ \text{ or } \ \mathbf{k}(\tau) - r = 0.$$

The matter distribution gives rise to physical quantities that are obtained from the Einstein field equations defined on the hypersurface Σ. In this framework, the Lanczos equations take the form

$$S^{\alpha}_{\beta} = \frac{\delta^{\alpha}_{\beta}\,\zeta^{\gamma}_{\gamma} - \zeta^{\alpha}_{\beta}}{8\pi}, \tag{49}$$

where $\zeta_{\alpha\beta} = K^{+}_{\alpha\beta} - K^{-}_{\alpha\beta}$ denotes the discontinuity in the extrinsic curvature across Σ.

In a perfect fluid scenario, the stress-energy tensor has the form $S^{\alpha}_{\beta} = \text{diag}[\rho, \mathcal{P}, \mathcal{P}]$, with ρ and $\mathcal{P}$ representing the surface energy density and pressure of the matter distribution.

The extrinsic curvature for the interior and exterior geometries is given by

$$K^{\pm}_{\alpha\beta} = -n^{\pm}_{\mu}\left[\frac{\partial^2 y^{\mu}_{\pm}}{\partial\eta^{\alpha}\,\partial\eta^{\beta}} + \Gamma^{\mu}_{\lambda\nu}\left(\frac{\partial y^{\lambda}_{\pm}}{\partial\eta^{\alpha}}\right)\left(\frac{\partial y^{\nu}_{\pm}}{\partial\eta^{\beta}}\right)\right], \tag{50}$$

where the unit normals to the hypersurface are represented by $n^{\pm}_{\mu}$.

One may express the unit normals explicitly as

$$n^{\mu}_{\pm} = \left(\frac{\dot{\mathbf{k}}}{\Phi_{\pm}(\mathbf{k})},\ \sqrt{\Phi_{\pm}(\mathbf{k}) + \dot{\mathbf{k}}^2},\ 0,\ 0\right). \tag{51}$$

Here, the overdot signifies differentiation relative to the proper time.

As a consequence of the Lanczos equations, we obtain

$$\sigma = \frac{[K^{\theta}_{\theta}]}{4\pi} = -\frac{\sqrt{\dot{\mathbf{k}}^2 - \frac{2m}{\mathbf{k}} + 1} - \sqrt{\dot{\mathbf{k}}^2 + 1 - \frac{R_S(\mathbf{k})}{\mathbf{k}}}}{4\pi\mathbf{k}}, \tag{52}$$

$$\mathcal{P} = \frac{[K^{\theta}_{\theta}] + [K^{\tau}_{\tau}]}{8\pi} = \frac{\mathbf{k}\big(R'_S(\mathbf{k}) - 2(\dot{\mathbf{k}}^2 + \ddot{\mathbf{k}}\mathbf{k} + 1)\big) + R_S(\mathbf{k})}{8\pi\mathbf{k}^2\sqrt{-\frac{R_S(\mathbf{k})}{\mathbf{k}} + \dot{\mathbf{k}}^2 + 1}} + \frac{2\big(\dot{\mathbf{k}}^2\mathbf{k} + \ddot{\mathbf{k}}\mathbf{k}^2 + \mathbf{k} - m\big)}{8\pi\mathbf{k}^2\sqrt{\dot{\mathbf{k}}^2 - \frac{2m}{\mathbf{k}} + 1}}, \tag{53}$$

$$2\mathcal{P} + \sigma = \frac{R'_S(\mathbf{k})\sqrt{\dot{\mathbf{k}}^2 - \frac{2m}{\mathbf{k}} + 1} - (\dot{\mathbf{k}}^2 + 2\ddot{\mathbf{k}}\mathbf{k} + 1)\sqrt{1 - \frac{R_S(\mathbf{k})}{\mathbf{k}} + \dot{\mathbf{k}}^2}}{4\pi\mathbf{k}\sqrt{-\frac{R_S(\mathbf{k})}{\mathbf{k}} + \dot{\mathbf{k}}^2 + 1}\,\sqrt{\dot{\mathbf{k}}^2 - \frac{2m}{\mathbf{k}} + 1}}. \tag{54}$$

The geometry is constructed under the assumption that the thin shell experiences no radial displacement at its equilibrium radius $\mathbf{k}_0$. It follows that the proper-time derivatives of the shell radius are identically zero, namely $\dot{\mathbf{k}}_0 = 0 = \ddot{\mathbf{k}}_0$.

Consequently, this yields

$$\sigma_0 = -\frac{1}{4\pi\mathbf{k}_0}\left\{\sqrt{\frac{2m}{\mathbf{k}_0} + 1} - \sqrt{\frac{b(\mathbf{k}_0)}{\mathbf{k}_0} + 1}\right\},$$

$$\mathcal{P}_0 = \frac{1}{8\pi\mathbf{k}_0^2}\left\{\frac{\mathbf{k}_0\left(R'_S(\mathbf{k}_0) - 2\right) + R_S(\mathbf{k}_0)}{\sqrt{1 - \frac{R_S(\mathbf{k}_0)}{\mathbf{k}_0}}} + \frac{2(\mathbf{k}_0 - m)}{\sqrt{1 - \frac{2m}{\mathbf{k}_0}}}\right\}.$$

$$\sigma_0 + 2\mathcal{P}_0 = \frac{R'_S(\mathbf{k}_0)\sqrt{1 - \frac{2m}{\mathbf{k}_0}} + \sqrt{1 - \frac{R_S(\mathbf{k}_0)}{\mathbf{k}_0}} - \sqrt{1 - \frac{2m}{\mathbf{k}_0}}}{4\pi\mathbf{k}_0\sqrt{1 - \frac{R_S(\mathbf{k}_0)}{\mathbf{k}_0}}\,\sqrt{1 - \frac{2m}{\mathbf{k}_0}}}. \tag{55}$$

At equilibrium, we denote the surface energy density by σ_0 and the corresponding pressure by $\mathcal{P}_0$. A negative value of σ_0 ($\sigma_0 < 0$) arises, implying that both the WEC and DEC are violated in this scenario. This violation indicates that the obtained configuration is supported by exotic matter. Such exotic matter distributions on the thin shell produce a repulsive effect that counteracts gravitational collapse and simultaneously keeps the WH throat open. Therefore, the constructed structure remains physically viable and is traversable for observers within this geometry.

We now proceed to investigate the stability of the constructed thin-shell WH geometry under small radial perturbations. To this end, we employ the linearized approach to analyze whether the configuration remains stable against such perturbations. To analyze the stability under radial perturbations at $\mathbf{k} = \mathbf{k}_0$, Eq. (52) yields the thin shell's equation of motion in the form

$$\mathcal{V}(\mathbf{k}) + \dot{\mathbf{k}}^2 = 0, \tag{56}$$

where $\mathcal{V}(\mathbf{k})$ corresponds to the effective potential function of the thin shell, given by

$$\mathcal{V}(\mathbf{k}) = 1 + \frac{m\,R_S(\mathbf{k})}{16\pi^2\mathbf{k}^4\sigma^2} - \frac{R_S(\mathbf{k})^2}{64\pi^2\mathbf{k}^4\sigma^2} - \frac{R_S(\mathbf{k})}{2\mathbf{k}} - \frac{m^2}{16\pi^2\mathbf{k}^4\sigma^2} - 4\pi^2\mathbf{k}^2\sigma^2 - \frac{m}{\mathbf{k}}. \tag{57}$$

Moreover, the conservation equation for energy is satisfied by the stress-energy tensor.

$$\frac{d}{d\tau}\Big(4\pi\mathbf{k}^2\sigma\Big) + \mathcal{P}\,\frac{d}{d\tau}\Big(4\pi\mathbf{k}^2\Big) = 0. \tag{58}$$

which simplifies to

$$\sigma' = -\frac{2}{\mathbf{k}}\Big(\mathcal{P}(\sigma) + \sigma\Big). \tag{59}$$

Since the thin shell is assumed to be in a static configuration at $k = k_0$, the stability analysis is performed in the neighborhood of this equilibrium point. Therefore, the effective potential $\mathcal{V}(k)$ can be locally approximated by its Taylor expansion around k_0, retaining terms up to second order. For the purpose of investigating the thin-shell stability, we

express the effective potential $\mathcal{V}(\mathbf{k})$ around the equilibrium radius $\mathbf{k}_0$ as a Taylor expansion centered at $\mathbf{k}_0$ is

$$\mathcal{V}(\mathbf{k}) = \mathcal{V}(\mathbf{k}_0) + \mathcal{V}'(\mathbf{k}_0)\,(\mathbf{k}-\mathbf{k}_0) + \tfrac{1}{2}\mathcal{V}''(\mathbf{k}_0)\,(\mathbf{k}-\mathbf{k}_0)^2 + \mathcal{O}\Big[(\mathbf{k}-\mathbf{k}_0)^3\Big]. \tag{60}$$

Since at equilibrium $\mathcal{V}(\mathbf{k}_0) = 0 = \mathcal{V}'(\mathbf{k}_0)$, the above relation reduces to

$$\dot{J}^2 + \omega^2 J^2 \simeq 0, \qquad J = \mathbf{k} - \mathbf{k}_0, \tag{61}$$

where the frequency parameter ω^2 is given by

$$\omega^2 = \frac{1}{2}\left.\frac{d^2\mathcal{V}}{d\mathbf{k}^2}\right|_{\mathbf{k}=\mathbf{k}_0}. \tag{62}$$

On performing differentiation of Eq. (61) with respect to τ, one finds

$$\ddot{J} + \omega^2 J \simeq 0. \tag{63}$$

The behavior of Eq. (63) depends on the sign of ω^2. If $\omega^2 > 0$, the solution corresponds to oscillations about the equilibrium position ($J = 0$), as illustrated in the left panel of Fig. 17, and hence the shell is stable. Therefore, the condition for stability is

$$\left.\frac{d^2\mathcal{V}}{d\mathbf{k}^2}\right|_{\mathbf{k}=\mathbf{k}_0} > 0. \tag{64}$$

When $\omega^2 < 0$, the shell radius expands exponentially, pointing to an unstable configuration, as depicted in the right panel of Fig. 17. The corresponding condition for instability can be written as

$$\left.\frac{d^2\mathcal{V}}{d\mathbf{k}^2}\right|_{\mathbf{k}=\mathbf{k}_0} < 0. \tag{65}$$

The developed configuration remains stable provided that $\mathcal{V}(\mathbf{k}_0) = 0 = \mathcal{V}'(\mathbf{k}_0)$. Consequently, we obtain

$$\mathcal{V}(\mathbf{k}) = \tfrac{1}{2}(\mathbf{k}-\mathbf{k}_0)^2\,\mathcal{V}''(\mathbf{k}_0). \tag{66}$$

The relation of the thin-shell mass and its radial derivatives to the energy density and pressure is as follows

$$\begin{aligned} M(\mathbf{k}_0) &= 4\pi\mathbf{k}_0^2\sigma_0,\\ M'(\mathbf{k}_0) &= -8\pi\mathbf{k}_0 p_0,\\ M''(\mathbf{k}_0) &= -8\pi\mathcal{P}_0 + 16\pi\xi_0^2\,(\sigma_0+\mathcal{P}_0), \end{aligned}$$

where $\xi_0^2 = \left.\frac{dp}{d\sigma}\right|_{\mathbf{k}=\mathbf{k}_0}$ represents the EoS parameter. Hence, we arrive at

$$\begin{aligned} \mathcal{V}''(\mathbf{k}_0) = -\frac{1}{2\mathbf{k}_0^4M^4}\Big\{ &-\mathbf{k}_0^4M(2m-R_S(\mathbf{k}_0))\\ &\Big(M''(2m-R_S(\mathbf{k}_0)) - 4M'R_S'(\mathbf{k}_0)\Big)\\ &+\mathbf{k}_0^4M^2\Big((R_S(\mathbf{k}_0)-2m)R_S''(\mathbf{k}_0) + \big(R_S'(\mathbf{k}_0)\big)^2\Big) + \mathbf{k}_0M^4\\ &\Big(\mathbf{k}_0R_S''(\mathbf{k}_0) - 2R_S'(\mathbf{k}_0) + (M')^2\Big) + 2R_S(\mathbf{k}_0) + 4m + 3\mathbf{k}_0^4(M')^2\\ &(R_S(\mathbf{k}_0)-2m)^2 + \mathbf{k}_0M^5\big(\mathbf{k}_0M'' - 4M'\big) + 3M^6\Big\}. \end{aligned} \tag{67}$$

With the aim of exploring the stability of the formulated model, we impose the condition $\mathcal{V}''(\mathbf{k}_0) > 0$. Substituting into Eq. (67), the inequality becomes

$$\begin{aligned} &-\Big(-\sigma_0(2m-R_S(\mathbf{k}_0))\Big)(32\pi\mathbf{k}_0\mathcal{P}_0R_S'(\mathbf{k}_0))\\ &+(2m-R_S(\mathbf{k}_0))\Big(16\pi\xi_0^2\\ &(\mathcal{P}_0+\sigma_0) - 8\pi\mathcal{P}_0\Big) + 48\pi\mathcal{P}_0^2(R_S(\mathbf{k}_0)-2m)^2\\ &+4\pi\mathbf{k}_0^2\sigma_0^2\Big((R_S(\mathbf{k}_0)-2m)R_S''(\mathbf{k}_0) + (R_S'(\mathbf{k}_0))^2\Big)\\ &+64\pi^3\mathbf{k}_0^4\Big(\mathbf{k}_0^2R_S''(\mathbf{k}_0) - 2\mathbf{k}_0R_S'(\mathbf{k}_0) + 2R_S(\mathbf{k}_0)\Big) + 64\pi^2\mathbf{k}_0^3p_0^2\\ &+4m + 2048\pi^5\mathbf{k}_0^6\sigma_0^6\Big((2\xi_0^2+3)\mathcal{P}_02\xi_0^2\sigma_0\Big)\\ &++3072\pi^5\mathbf{k}_0^6\sigma_0^6\,(128\pi^3\mathbf{k}_0^6\sigma_0^4)^{-1} > 0. \end{aligned} \tag{68}$$

Furthermore, the stability constraints can be expressed in the following form

$$\mathcal{V}''(\mathbf{k}_0) > 0 \quad\Rightarrow\quad \tau(h_0)\xi_0^2 - \vartheta_0 > 0. \tag{69}$$

Here, the coefficient associated with the EoS parameter written as $\tau(\mathbf{k}_0) = \tau_0$, while the remaining terms are denoted by $\vartheta_{\mathbf{k}_0} = \vartheta_0$.

The stability regions, which outline the thin shell's geometry, are formulated as

1. For $\tau_0 < 0 \quad\Rightarrow\quad \xi_0^2 < \dfrac{\vartheta_0}{\tau_0}$.
2. For $\tau_0 > 0 \quad\Rightarrow\quad \xi_0^2 > \dfrac{\vartheta_0}{\tau_0}$.

Here, ϑ_0 is defined as

$$\begin{aligned} \vartheta_0 = R_S(\mathbf{k})\Big(&8\big(m\mathcal{P}_0(6\mathcal{P}_0\\ &+\sigma_0) - 4\pi^2\mathbf{k}_0^3\sigma_0^4\big) - \mathbf{k}_0\sigma_0\big(\mathbf{k}_0\sigma_0R_S''(\mathbf{k}_0)\\ &+8\mathcal{P}_0R_S'(\mathbf{k}_0)\big) + \mathbf{k}_0\sigma_0\big(2\mathbf{k}_0\sigma_0R_S''(\mathbf{k}_0)(m-8\pi^2\mathbf{k}_0^3\sigma_0^2)\big)\\ &+R_S'(\mathbf{k}_0)\big(-\mathbf{k}_0\sigma_0R_S'(\mathbf{k}_0) + 32\pi^2\mathbf{k}_0^3\sigma_0^3 + 16m\mathcal{P}_0\big)\\ &-2\mathcal{P}_0R_S(\mathbf{k}_0)^2(6\mathcal{P}_0+\sigma_0) - 8\Big(32\pi^4\\ &\mathbf{k}_0^6\sigma_0^4\big(4\mathcal{P}_0^2 + 6\mathcal{P}_0\sigma_0 + 3\sigma_0^2\big)\Big)\Big) \end{aligned}$$

$$+8\pi^2\mathbf{k}_0^3 m\sigma_0^4 + m^2 P_0\,(6P_0+\sigma_0)\,. \tag{70}$$

$$\tau_0 = 4\sigma_0(P_0+\sigma_0)$$
$$\left[4mR_S(\mathbf{k}_0) - R_S(\mathbf{k}_0)^2 + 256\pi^4\mathbf{k}_0^6\sigma_0^4 - 4m^2\right].$$

The analysis of the thin shell encompassing the WH geometry is carried out by identifying the stable regions associated with the different shape functions.

To investigate stability, the analysis is carried out using τ_0 and the ratio ϑ_0/τ_0. Whenever τ_0 takes negative values, the thin-shell system exhibits stability. These stable regions are marked as light pink shaded zones in the figs. (see Figs. 18, 19, 20). Whenever τ_0 takes positive values, the shell exhibits stability, which is indicated by the light green region in the plot. Among all the parameters, stability is found to be most sensitive to variations in m. For case I, $m = 0.41$ and $m = 0.43$, increase in m compresses the colored stability zones and shifts the stability threshold upward, particularly in the higher regions of the plots (Fig. 18) as well as for case II in Figs. 19 and 20 case III respectively. This effect sharpens the effective potential at k_0, eliminating nearby minima and thus increasing the probability of collapse or runaway expansion. For all cases, the shaded regions indicate the parameter ranges where stable solutions exist.

5 Summary and results

- Interstellar travel, whether across immense cosmic distances within a universe or between different universes, could be made feasible by using a theoretical shortcut called a WH. Such a structure represents a tunnel, or throat, through which two distant points of spacetime can be joined, linking asymptotically flat regions while avoiding the formation of an event horizon.
- It is observed that the shape functions derived under the influence of nonzero tidal forces, null complexity, and the TOV condition conform to the Morris–Thorne requirements for a physically acceptable WH. The plots corresponding to the different properties in case I, case II, and case III are shown in Figs. 1, 5, and 9, respectively.
- The choice of a redshift function $\Phi(r)$ consisting of tidal forces introduces additional contributions to the field equations through its first and second derivatives. These terms modify the relation between geometry and matter fields, which in turn influences the dynamical stability of the configuration. Consequently, the stability of the WH, especially under small fluctuations, depends on the radial dependence of $\Phi(r)$. From the perspective of gravitational lensing, the redshift function has a direct impact on the effective optical geometry. In the constant case, the deflection angle often points to a repulsive character of the WH. However, allowing $\Phi(r)$ to vary can alter this signature by reinforcing, softening, or reversing lensing behavior.
- Furthermore, all energy conditions have been illustrated in Figs. 1, 2, 3, 4, 5, 6, 7, 8, 9, 10, 11 and 12 for all cases. Interestingly, traversable WHs in teleparallel gravity can only be realized with exotic matter, whose central role lies in ensuring the violation of the NEC. Across all of the shape functions, the graphs of the energy conditions display domains of positivity as well as negativity.
- The embedded diagrams corresponding to these shape functions for the upper and lower universes are displayed in Fig. 13 for all cases, respectively.
- In continuation, we examined the requisite quantity of exotic matter to maintain these WHs through the framework of the VIQ in Fig. 14.
- As shown in Fig. 15, the deflection angle exhibits variation with the impact parameter. r_c across multiple parameter values.
- Beyond the analysis of energy conditions, Fig. 16 depicts the effective potential V_{eff} for timelike ($\epsilon = -1$) geodesics, plotted for various values of angular momentum L, while non-zero redshift functions and $m = 1$. These plots yield valuable information about the trajectories of test particles in the given spacetime, highlighting the distinctions in potential wells and barrier structures. The stability of the developed structure depends on ω^2 is discussed in Fig. 17.
- The thin-shell stability for all cases is analyzed using the conditions of τ_0 and ξ_0^2, where the shaded regions in Figs. 18, 19 and 20 represent the stable domains. For both models, the parameter m plays a crucial role in stability: higher values of m reduce the stability regions and enhance the chance of instability, while lower values enlarge these regions and improve the viability of thin-shell WHs.
- Although the present work is theoretical, the obtained WH solutions can be associated with potential observational consequences. In particular, the spacetime geometry of a WH can significantly alter the propagation of light, leading to gravitational lensing effects that are qualitatively different from those produced by black holes, such as enhanced light deflection, distorted Einstein rings, or the appearance of additional images. These features may serve as indirect signatures of WH geometries in astrophysical observations. Furthermore, the violation of energy conditions required to sustain the WH throat can, in principle, be constrained by observational bounds on compact objects and large-scale gravitational phenomena. Within modified gravity theories, such violations may arise from effective geometric terms rather than exotic matter sources, thereby improving the phys-

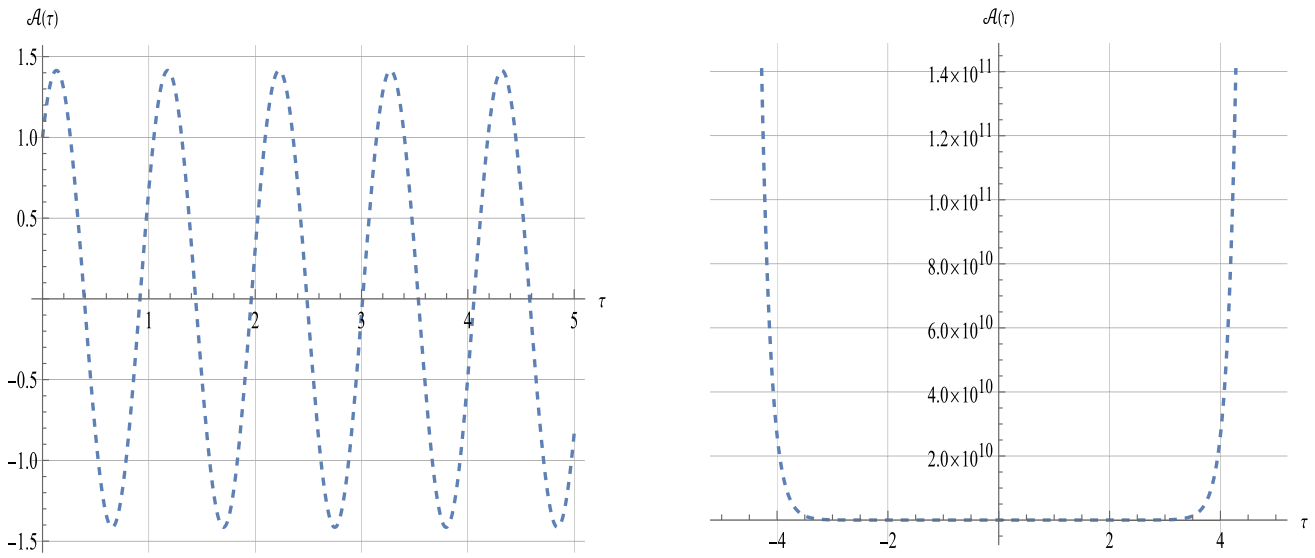

Fig. 17 Variation pattern of $\mathcal{A}$ in terms of the proper time τ for the exponential solution ($\zeta^2 = -36$) of Eq. (63), illustrating the unbounded growth of perturbations that renders the thin-shell WH throat unstable

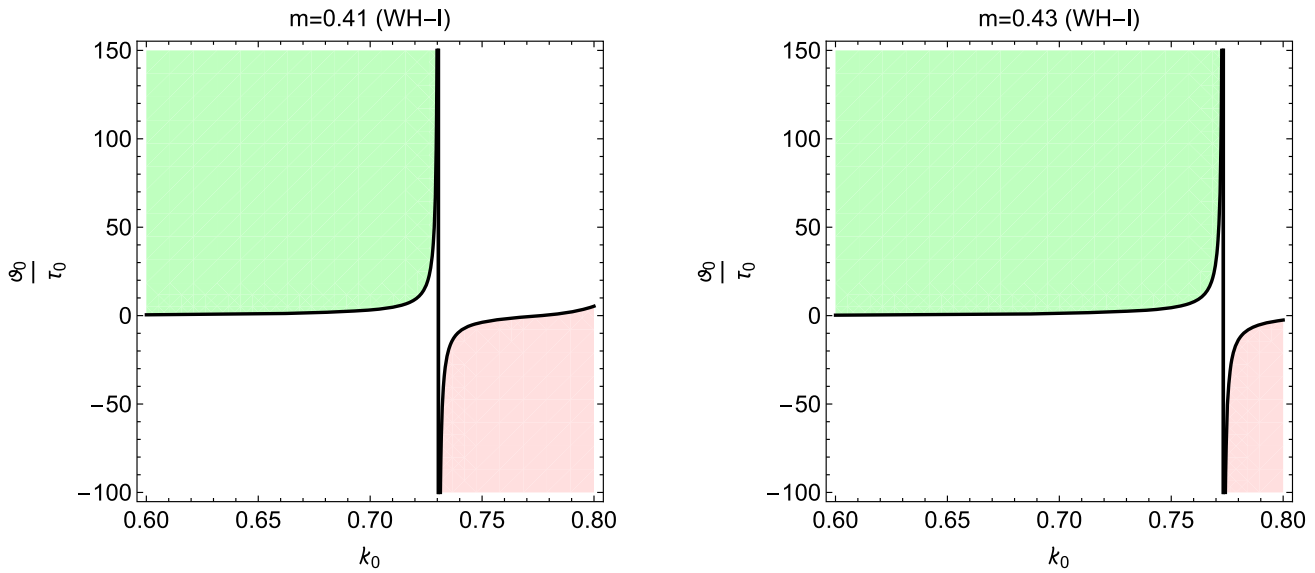

Fig. 18 Evolution of the ϑ_0/τ_0 w.r.t $\mathbf{k}_0$ for $m = 0.41$ and $m = 0.43$

ical viability of the WH configurations discussed in this work.

Acknowledgements Sweeti Kiroriwal thanks the University Grants Commission (UGC), New Delhi, India, for awarding the Senior Research Fellowship (UGC-Ref No.: 211610000030). S. K. Maurya conveys his sincere thanks to the University of Nizwa, Oman, for their continued encouragement. Jitendra Kumar acknowledges the authorities of the Central University of Haryana (CUH) for their support.

Data Availability Statement This article does not involve any associated data and will not be deposited. All necessary calculations and graphical analyses are fully contained in the manuscript. [Authors' comment: This is a theoretical work and no new code/software has been generated. The numerical computation has been performed by using mathematica and python.].

Code Availability Statement This manuscript has no associated code/software. [Authors' comment: Code/Software sharing not applicable to this article as no code/software was generated or analysed during the current study. The current work has already included a comprehensive analysis and the corresponding calculations.].

Declarations

Conflict of interest The authors declare no competing financial or non-financial interests.

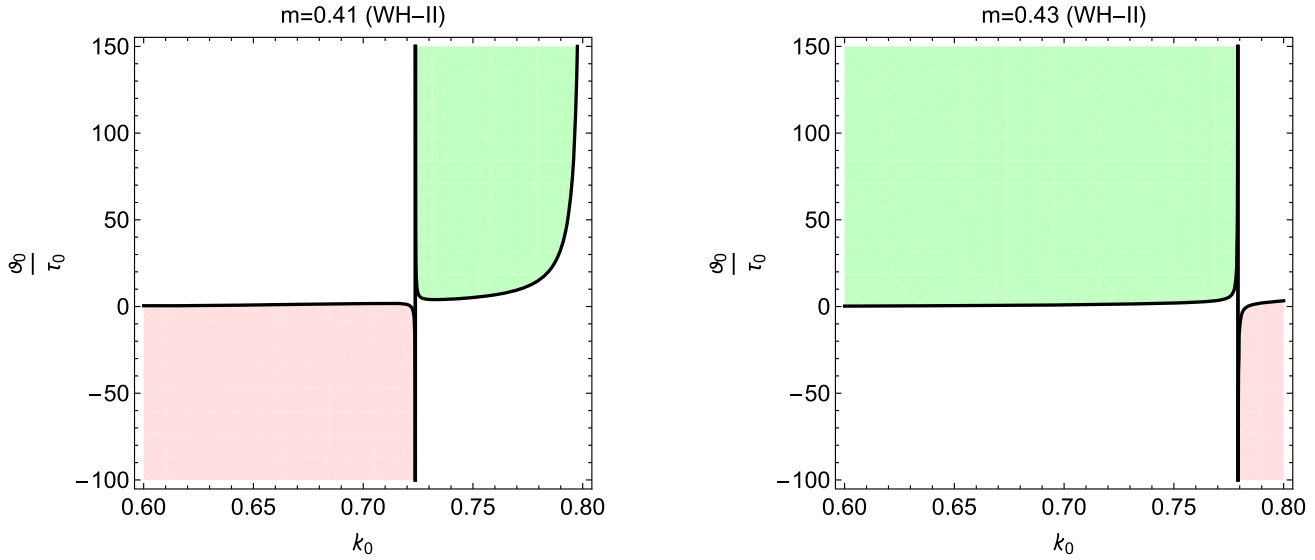

Fig. 19 Evolution of the ϑ_0/τ_0 w.r.t $\mathbf{k}_0$ for $m = 0.41$ and $m = 0.43$

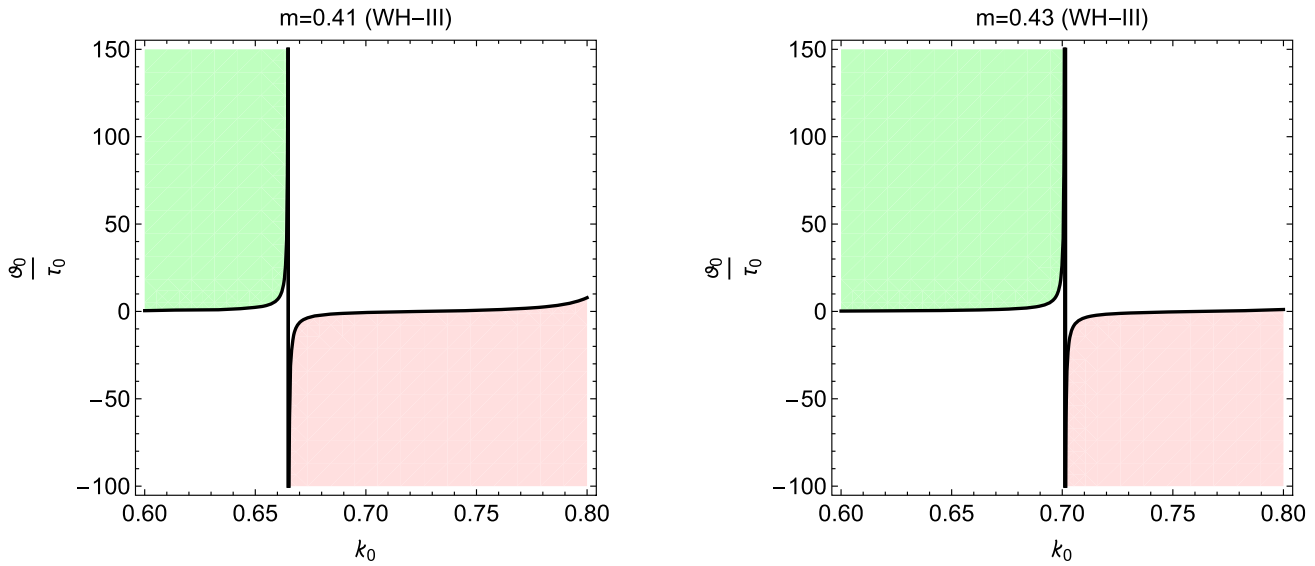

Fig. 20 Evolution of the ϑ_0/τ_0 w.r.t $\mathbf{k}_0$ for $m = 0.41$ and $m = 0.43$

Funded by SCOAP[3].

References

1. L. Flamm, Republication of: Contributions to Einstein's theory of gravitation. Gen. Relativ. Gravit. **47**(2015), 72 (2015). https://doi.org/10.1007/s10714-015-1908-2
2. A. Einstein, N. Rosen, The particle problem in the general theory of relativity. Phys. Rev. D **48**, 73–77 (1935)
3. C.W. Misner, J.A. Wheeler, Ann. Phys. **2**, 525–603 (1957). https://doi.org/10.1016/0003-4916(57)90049-0
4. J.A. Wheeler, Phys. Rev. **97**, 511–536 (1955). https://doi.org/10.1103/PhysRev.97.511
5. R.W. Fuller, J.A. Wheeler, Phys. Rev. **128**, 919–929 (1962). https://doi.org/10.1103/PhysRev.128.919
6. H.G. Ellis, J. Math. Phys. **14**, 104–118 (1973). https://doi.org/10.1063/1.1666161

7. S. Kar, Phys. Rev. D **49**, 862–865 (1994). https://doi.org/10.1103/PhysRevD.49.862
8. M.S. Morris, K.S. Thorne, Am. J. Phys. **56**, 395–412 (1988). https://doi.org/10.1119/1.15620
9. M. Visser,
10. V. Khatsymovsky, Phys. Lett. B **320**, 234–240 (1994). https://doi.org/10.1016/0370-2693(94)90650-5
11. H.A. Shinkai, S.A. Hayward, Phys. Rev. D **66**, 044005 (2002). https://doi.org/10.1103/PhysRevD.66.044005
12. A.G. Riess, L.G. Strolger, S. Casertano, H.C. Ferguson, B. Mobasher, B. Gold, P.J. Challis, A.V. Filippenko, S. Jha, W. Li et al., Astrophys. J. **659**, 98–121 (2007). https://doi.org/10.1086/510378
13. S. Perlmutter et al. [Supernova Cosmology Project], Astrophys. J. **517**, 565–586 (1999). https://doi.org/10.1086/307221
14. A.A. Starobinsky, Phys. Lett. B **91**, 99–102 (1980). https://doi.org/10.1016/0370-2693(80)90670-X
15. T. Harko, F.S.N. Lobo, S. Nojiri, S.D. Odintsov, Phys. Rev. D **84**, 024020 (2011). https://doi.org/10.1103/PhysRevD.84.024020
16. J.B. Jiménez, L. Heisenberg, T. Koivisto, Phys. Rev. D **98**(4), 044048 (2018). https://doi.org/10.1103/PhysRevD.98.044048
17. R. Lazkoz, F.S.N. Lobo, M. Ortiz-Baños, V. Salzano, Phys. Rev. D **100**(10), 104027 (2019). https://doi.org/10.1103/PhysRevD.100.104027
18. S. Mandal, P.K. Sahoo, J.R.L. Santos, Phys. Rev. D **102**(2), 024057 (2020). https://doi.org/10.1103/PhysRevD.102.024057
19. G.N. Gadbail, S. Mandal, P.K. Sahoo, Phys. Lett. B **835**, 137509 (2022). https://doi.org/10.1016/j.physletb.2022.137509
20. Z. Hassan, S. Ghosh, P.K. Sahoo, V.S.H. Rao, Gen. Relativ. Gravit. **55**(8), 90 (2023). https://doi.org/10.1007/s10714-023-03139-y
21. G. Mustafa, Z. Hassan, P.H.R.S. Moraes, P.K. Sahoo, Phys. Lett. B **821**, 136612 (2021). https://doi.org/10.1016/j.physletb.2021.136612
22. T. Harko, T.S. Koivisto, F.S.N. Lobo, G.J. Olmo, D. Rubiera-Garcia, Phys. Rev. D **98**(8), 084043 (2018). https://doi.org/10.1103/PhysRevD.98.084043
23. A. Bassi, S.A. Adil, M.P. Rajvanshi, A.A. Sen, Eur. Phys. J. C **83**(6), 525 (2023). https://doi.org/10.1140/epjc/s10052-023-11707-4
24. A. Sahoo, S.K. Tripathy, B. Mishra, S. Ray, Eur. Phys. J. C **84**(3), 325 (2024). https://doi.org/10.1140/epjc/s10052-024-12638-4
25. A. Banerjee, A. Pradhan, T. Tangphati, F. Rahaman, Eur. Phys. J. C **81**(11), 1031 (2021). https://doi.org/10.1140/epjc/s10052-021-09854-7
26. F.S.N. Lobo, M.A. Oliveira, Phys. Rev. D **80**, 104012 (2009). https://doi.org/10.1103/PhysRevD.80.104012
27. N.M. Garcia, F.S.N. Lobo, Phys. Rev. D **82**, 104018 (2010). https://doi.org/10.1103/PhysRevD.82.104018
28. N. Rahman, M. Kalam, A. Das, S. Islam, F. Rahaman, M. Murshid, Eur. Phys. J. Plus **138**(2), 146 (2023). https://doi.org/10.1140/epjp/s13360-023-03764-1
29. M. Kalam, A. Ghari, I. Radinschi, H. Haghi, F. Rahaman, T. Chowdhury, New Astron. **113**, 102288 (2024). https://doi.org/10.1016/j.newast.2024.102288
30. A. Malik, F. Mofarreh, A. Zia, A. Ali, Chin. Phys. C **46**(9), 095104 (2022). https://doi.org/10.1088/1674-1137/ac74b0
31. P. Bhar, A. Ditta, A. Errehymy, Nucl. Phys. B **1006**, 116621 (2024). https://doi.org/10.1016/j.nuclphysb.2024.116621
32. V. De Falco, E. Battista, S. Capozziello, M. De Laurentis, Eur. Phys. J. C **81**(2), 157 (2021). https://doi.org/10.1140/epjc/s10052-021-08958-4
33. C.G. Boehmer, T. Harko, F.S.N. Lobo, Phys. Rev. D **85**, 044033 (2012). https://doi.org/10.1103/PhysRevD.85.044033
34. M. Sharif, A. Ikram, Int. J. Mod. Phys. D **24**(01), 1550003 (2014). https://doi.org/10.1142/S0218271815500030
35. A.G. Agnese, M. La Camera, Phys. Rev. D **51**, 2011–2013 (1995). https://doi.org/10.1103/PhysRevD.51.2011
36. E.F. Eiroa, M.G. Richarte , C. Simeone, Phys. Lett. A **373**, 1–4 (2008). https://doi.org/10.1016/j.physleta.2008.10.065. [erratum: Phys. Lett. 373, 2399-2400 (2009)]
37. L.A. Anchordoqui, S.E. Perez Bergliaffa, D.F. Torres, Phys. Rev. D **55**, 5226–5229 (1997). https://doi.org/10.1103/PhysRevD.55.5226
38. K.K. Nandi, B. Bhattacharjee, S.M.K. Alam, J. Evans, Phys. Rev. D **57**, 823–828 (1998). https://doi.org/10.1103/PhysRevD.57.823
39. F. Rahaman, N. Rahman, M. Kalam, M. Murshid, A. Das, S. Islam, S. Das, Gen. Relativ. Gravit. **57**(2), 40 (2025). https://doi.org/10.1007/s10714-025-03371-8
40. R. Sengupta, S. Ghosh, M. Kalam, S. Ray, Class. Quantum Gravity **39**(10), 105004 (2022). https://doi.org/10.1088/1361-6382/ac61ae
41. S. Mandal, D. Wang, P.K. Sahoo, Phys. Rev. D **102**, 124029 (2020). https://doi.org/10.1103/PhysRevD.102.124029
42. F. Parsaei, S. Rastgoo, P.K. Sahoo, Eur. Phys. J. Plus **137**(9), 1083 (2022). https://doi.org/10.1140/epjp/s13360-022-03298-y
43. M. Chakraborty, S. Chakraborty, J. Subat. Part. Cosmol. **1–2**, 100006 (2024). https://doi.org/10.1016/j.jspc.2024.100006
44. M.R. Mehdizadeh, M. Kord Zangeneh, F.S.N. Lobo, Phys. Rev. D **91**(8), 084004 (2015). https://doi.org/10.1103/PhysRevD.91.084004
45. S. Halder, S. Bhattacharya, S. Chakraborty, Phys. Lett. B **791**, 270–275 (2019). https://doi.org/10.1016/j.physletb.2019.02.041
46. T. Bandyopadhyay, S. Chakraborty, Class. Quantum Gravity **26**, 085005 (2009). https://doi.org/10.1088/0264-9381/26/8/085005
47. S. Chakraborty, M. Chakraborty, Phys. Scripta **99**(10), 105033 (2024). https://doi.org/10.1088/1402-4896/ad75c8
48. A. Dutta, D. Roy, N.J. Pullisseri, S. Chakraborty, Eur. Phys. J. C **83**(6), 500 (2023). https://doi.org/10.1140/epjc/s10052-023-11681-x
49. K. Jusufi, A. Banerjee, S.G. Ghosh, Eur. Phys. J. C **80**(8), 698 (2020). https://doi.org/10.1140/epjc/s10052-020-8287-x
50. B. Ghosh, S. Mitra, S. Chakraborty, Mod. Phys. Lett. A **36**(05), 05 (2021). https://doi.org/10.1142/S0217732321500243
51. S. Chakraborty, M. Chakraborty, Eur. Phys. J. C **84**(9), 915 (2024). https://doi.org/10.1140/epjc/s10052-024-13305-4
52. S. Chakraborty, M. Chakraborty, Int. J. Geom. Methods Mod. Phys. **21**(10), 2440018 (2024). https://doi.org/10.1142/S0219887824400188
53. D. Zhao, Eur. Phys. J. C **82**(4), 303 (2022). https://doi.org/10.1140/epjc/s10052-022-10266-4
54. W. Wang, H. Chen, T. Katsuragawa, Phys. Rev. D **105**(2), 024060 (2022). https://doi.org/10.1103/PhysRevD.105.024060
55. L. Herrera, A. Di Prisco, J. Ospino, Phys. Rev. D **98**(10), 104059 (2018). https://doi.org/10.1103/PhysRevD.98.104059
56. L. Herrera, Phys. Rev. D **97**(4), 044010 (2018). https://doi.org/10.1103/PhysRevD.97.044010
57. S. Bhattacharya, S. Nalui, J. Math. Phys. **64**(5), 052501 (2023). https://doi.org/10.1063/5.0148762
58. R.C. Tolman, Phys. Rev. **55**, 364–373 (1939). https://doi.org/10.1103/PhysRev.55.364
59. J.R. Oppenheimer, G.M. Volkoff, Phys. Rev. **55**, 374–381 (1939). https://doi.org/10.1103/PhysRev.55.374
60. D. Marolf, Gen. Relativ. Gravit. **31**, 919–944 (1999). https://doi.org/10.1023/A:1026646507201
61. P. Collas, D. Klein, Am. J. Phys. **80**, 203–210 (2012). https://doi.org/10.1119/1.3672848
62. K.S. Virbhadra, G.F.R. Ellis, Phys. Rev. D **62**, 084003 (2000). https://doi.org/10.1103/PhysRevD.62.084003
63. C.M. Claudel, K.S. Virbhadra, G.F.R. Ellis, J. Math. Phys. **42**, 818–838 (2001). https://doi.org/10.1063/1.1308507
64. K.S. Virbhadra, D. Narasimha, S.M. Chitre, Astron. Astrophys. **337**, 1–8 (1998). arXiv:astro-ph/9801174

65. V. Bozza, Phys. Rev. D **66**, 103001 (2002). https://doi.org/10.1103/PhysRevD.66.103001
66. J.P.S. Lemos, F.S.N. Lobo, S. Quinet de Oliveira, Phys. Rev. D **68**, 064004 (2003). https://doi.org/10.1103/PhysRevD.68.064004
67. J.M. Tejeiro S., E.A. Larranaga R., Rom. J. Phys. **57**, 736-747 (2012). arXiv:gr-qc/0505054
68. C.W. Misner, K.S. Thorne, J.A. Wheeler, *Gravitation* (W.H. Freeman and Company, San Francisco, 1973)
69. B.F. Schutz, *A First Course in General Relativity* (Cambridge University Press, Cambridge, 2014)
70. S. Panpanich, S. Ponglertsakul, L. Tannukij, Phys. Rev. D **100**(4), 044031 (2019). https://doi.org/10.1103/PhysRevD.100.044031
71. R. Shaikh, P. Banerjee, S. Paul , T. Sarkar, JCAP **07**, 028 (2019). https://doi.org/10.1088/1475-7516/2019/07/028. [erratum: JCAP 12, E01 (2023)]